

**Chapter III:**

**Fluid Source-based Modeling of Melt Initiation within  
the Subduction Zone Mantle Wedge: Implications for  
Geochemical Trends in Arc Lavas**

Laura Baker Hebert and Paul Asimow

**Abstract**

This study supplements GyPSM-S modeling (Chapter 2) with a focus on the influences of slab fluid source lithology and fluid transport mechanisms on melt geochemistry, the implications of mantle source depletion related to fluid fluxing, and potential melt migration processes. Slab age and convergence velocity, which contribute to the slab thermal structure, are significant for the locations of dehydration reactions within the different lithological layers of the slab. The fluid source lithology determines the fluid flux and the fluid-mobile trace element input to the wedge. Through an investigation of changing fluid inputs based on changing subduction model parameters, there is a progression of geochemical characteristics described in studies of cross-arc and along-arc lavas that can be duplicated assuming (i) limited fluid-rock interaction within the mantle wedge and (ii) melt migration preserves the spatial distinction among melts initiated in different areas of the wedge. Specifically, volcanic front lavas have significant contributions from shallower slab fluid sources, and rear-arc lavas have significant contributions from deeper slab fluid sources. Evidence for limited fluid-rock interaction could imply either a rapid fluid transport mechanism or a fluid-dominated trace element budget within the low-viscosity channel (LVC). Although we do not explicitly include a back-arc in these models, interpretations of the results lead to several potential mechanisms to explain hydrous inputs to back-arc source regions.

**Keywords:** Costa Rica, Izu-Bonin, subduction, volcanic front, cross-arc trends, trace element, GyPSM-S

## 1. Introduction

Melt initiation within the mantle at plate boundaries is an important problem that has been addressed through analyses of lavas and xenoliths collected at the surface, interpretations of seismic imaging results, and experimental investigations [1-5]. Spreading centers at divergent boundaries represent the most accessible environment, due to well-established estimates of N-MORB-source mantle composition and decompression pathways, a lack of significant crustal contamination, and agreement amongst experimental results [6, 7]. At convergent boundaries, the story is complicated by fluxing of the mantle by components derived from heterogeneous slab sources, the potential for significant crustal contamination, sources of initial and progressive mantle source depletion, and a more complex pressure and temperature structure.

Major element abundances in arc lavas are derived from partial melting of the wedge peridotite above the slab, but large-ion lithophile elements (LILE) and other incompatible elements can be traced to slab-derived influences such as sediment melting [8, 9], dehydration of the altered oceanic crust (AOC) [10], and/or dehydration of subducting serpentized lithosphere [11, 12]. In general, convergent margins involve lavas that are enriched in incompatible fluid-mobile elements (Rb, Ba, U, K, Sr, Pb) and depleted in incompatible high field strength elements (HFSE) (Nb, Zr, Ta) and heavy rare-earth elements (HREE) [13-15; others], suggesting a significant connection between fluids, mantle source bulk composition, and melt production. However, interpretation of the geochemistry can be somewhat obscured by the complexity of slab sources.

The depth interval and the magnitude of fluid release from the subducting plate are

a function of parameters such as slab age and convergence velocity (Chapter 2) as well as the composition of the descending plate [16]. Specifically, the different lithological fluid sources emphasized by different subduction parameters allow for changing fluid addition patterns (mass and fluid-mobile trace element chemistry) along the length of the subducting plate through the upper mantle [16, 17]. These patterns may directly influence the composition and mass fraction of fluxed melts within the wedge, leading to regional variations in arc lava geochemistry. Variations can be compared among different subduction systems, or through cross-arc and along-arc trends within the same subduction system. For example, relative contributions from heterogeneous slab fluid sources can be manifested in diverse chemical characteristics of lavas derived from different depths above the seismic Wadati-Benioff zone (WBZ) [15, 18, 19].

Interpretations of arc lava geochemistry include the potential for re-melting of previously depleted sources as an explanation for significant HFSE and HREE depletions. Sequential melting within the system, such as at a back-arc spreading center, has been invoked as a cause; however, some systems, such as the northern Izu-Bonin subduction zone, do not involve current back-arc spreading and still maintain such depletions [33]. It has been proposed that hydrous fluid addition process alone may be somehow responsible for these trends [68].

GyPSM-S (**G**eodynamic and **P**etrological **S**ynthesis **M**odel for Subduction, Chapter 2) involves the dehydration of a subducting slab and the impact of fluid release on the shallow (< 200 km) mantle wedge, assuming an equilibrium-based interaction. The primary model observation is the development of a water-saturated low-viscosity channel (LVC), which arises due to the partitioning of water into nominally-anhydrous minerals

(NAM), the thermal structure of the mantle wedge, and the down-dip advection of near-slab material (Chapter 2). Water in NAM has two consequences: reduction of the peridotite solidus [5, 20], and reduction of solid matrix viscosity [21]. The thickness of the LVC, which can reach tens of kilometers, separates the slab-wedge interface from the water-saturated peridotite solidus. Similar displacements between the slab surface and the zone of active melting have been imaged seismically, and are well established by previous models [16, 17, 22]. In GyPSM-S, the locations of melting are strongly determined by the positions of fluid release from dehydration reactions within hydrated slab layers, given a vertical buoyancy-driven fluid migration path.

The use of the pHMELTS algorithm [20, 27, 28] in the structure of GyPSM-S allows for major and trace element analyses of melts and residues and includes a treatment of water (H<sub>2</sub>O) as a trace element. However, analyses are somewhat limited in that pHMELTS cannot yet account for fluid-mobile trace elements carried with the hydrous species from the slab. Additionally, specific tracing of fluids as direct influences on melt composition is complicated by the slight smearing within GyPSM-S due to iterative particle-to-node interpolation steps, mostly observed in water mass and leading to lower instantaneous melt fractions (Chapter 2). In order to demonstrate the applicability of GyPSM-S results to actual datasets, a supplemental modeling approach is required to account for the addition of these important fluid-mobile tracers and to make detailed inferences as to the geochemistry of arc lavas with respect to slab fluid sources and as a function of changing subduction parameters.

Melt migration processes are neglected in the current formulation of GyPSM-S, which assumes a near-fractional melt extraction scheme and a lack of interaction of

extracted melt with the solid matrix. However, theoretical treatment of the extracted melts through the established pressure-temperature structure of the wedge is possible. Past studies have suggested mechanisms by which melt generated within the mantle at plate boundaries can transit to the surface. Within the context of convergent boundaries, Spiegelman and McKenzie [23] describe porous flow driven by pressure gradients as a mechanism of melt focusing towards the wedge corner, Hall and Kincaid [24] invoke diapirism of melts towards the overlying lithosphere, and Furukawa [25] proposes fracture propagation as a mechanism of melt extraction. Kelemen et al. [26, and references therein] additionally discuss the role of dissolution channels in melt migration at mid-ocean ridges, resulting in a combination of rapid, chemically-isolated melt flow and porous reactive flow. The processes of melt migration can be very significant with regard to understanding trends observed within subduction systems, considering the locations of melt initiation within the wedge and geochemistry of the initial melts as strongly dependent on the identity of slab-derived fluid sources (Chapter 2) [2].

This study represents an extension of a fully-integrated geochemical and geodynamical approach (GyPSM-S) to specific mass tracing. A fluid source-based approach is employed to determine how slab dehydration changes with changing subduction model parameters and how this influences the major and trace element chemistry of fluid-fluxed melts within the wedge. In addition to a fully-equilibrated pathway of fluid migration, we also consider the consequences of less-interactive fluid paths through the near-slab wedge. Cross-arc and along-arc variations in regional geochemical datasets are compared to the model results, with an emphasis on changing slab fluid-source lithology. Additionally, we offer a discussion of simple melt migration

scenarios which may preserve relative heterogeneities in melts initiated at different locations within the wedge.

## **2. Model Parameters and Regional Significance**

Results from GyPSM-S modeling indicate that the first-order control on the locations of fluid release from the slab (and therefore, the locations of melt production in the mantle wedge) is the slab thermal structure, primarily defined by slab age and secondarily by convergence velocity. More mature slabs have significantly different patterns of fluid release than younger slabs (Chapter 2). While examining the dehydration structures produced by GyPSM-S over a range of subduction parameter space, we chose to focus this study on two systems with different slab thermal structures to more closely examine the potential implications of the different fluid release patterns for melt production and chemistry.

The Northern Izu-Bonin intra-oceanic subduction system (NIB, Table 3) involves the mature Pacific plate (135 Ma) subducting beneath the Philippine Sea plate at a relatively moderate convergence velocity (~5.0 cm/yr) and a moderate dip angle of 45° [29]. The arc itself includes a volcanic front, extensional zones, and seamount chains towards the rear-arc trending into the Shikoku Basin [19]. The history of the arc involves a multi-stage process [30-33]. There are two periods of arc formation associated with the IBM system: Eocene-Oligocene volcanism and mid-Miocene to present [31]. A hiatus of around 7.5 Ma between these periods [34] involved rifting associated with the Shikoku Basin [31]. The end of the Oligocene marks the end of boninitic lava appearance within

the arc record, and the completion of the sub-arc mantle "replacement" stage from an ultra-depleted mantle to depleted Indian MORB-source mantle [31]. With resumption of volcanic activity in the mid-Miocene, a quasi-steady-state flow was established within the wedge characterized by (i) continuous advection of Indian MORB-source mantle from the rear-arc that is (ii) continuously fluxed by hydrous slab components, leading to (iii) constancy within temporal trends of major element oxides [31]. Straub [31] therefore suggests that melt formation processes and the source composition are relatively constant in this system and that the thin (~7-22 km) crust does not seem to have a significant impact on lava chemistry. The volcanic front (VF) of the Izu-Bonin arc is one of the most depleted of all volcanic arcs, and there exist significant cross-arc variations in the geochemistry of erupted lavas, including  $\epsilon_{Nd}$ , Ba/Nb, U/Nb, and  $^{87}Sr/^{86}Sr$  [19]. Additionally, there is a lack of evidence of slab-derived sediment melting influence to the shallow (< 175 km depth) wedge [19, 35] which emphasizes the role of fluids in the production and geochemistry of melts.

The central Costa Rican subduction system (CCR, Table 3), on the southeastern end of the Central American arc, involves the subduction of the relatively young Cocos plate beneath the Caribbean plate along the Middle America Trench at moderately fast convergence velocity (~9.0 cm/yr) and a moderate dip angle of 45° [36]. The Central American system involves systematic along-arc variations in many geochemical indicators such as  $\delta^{18}O$  [37], U/Th, Ba/La, and  $Na_{6.0}$ . These variations have been linked to geophysical parameters such as slab dip, crustal thickness, and slab composition that vary along arc strike [16, 38-41]. Specifically, it has been concluded that the concentration of trace elements contributed by the slab-derived fluids reaches a minimum beneath the Costa

Rican segment [39, 42, 43] and that the degree of melting is relatively lower beneath Costa Rica [39]. Rupke et al. [16] speculate on the basis of geodynamic modeling that there is a lack of a strong serpentinite-derived fluid release beneath Costa Rica, contributing to the along-arc geochemical differences.

### **3. Method**

#### *3.1. Initial GyPSM-S calculation of the shallow hydrated wedge*

We used GyPSM-S (see Chapter 2 for full model description) to describe the thermal structure and locations of slab dehydration for subduction model parameters (slab age, convergence velocity, slab dip angle) approximating six regional systems, respectively (Table 3). Results for each model were taken from a GyPSM-S iteration representing ~160-280 kyr of subduction, upon water-saturation of the LVC and initiation of active melting regions, to avoid potential errors due to nodal smearing. The initial fluid transient is avoided, and the locations of fluid release from the slab have been shown not to change appreciably over full model run durations (two to five million years).

#### *3.2. Construction of calculation columns*

In order to address the important issue of fluid-mobile tracers that are carried with the hydrous fluid phase and are neglected in the current formulation of pHMELTS, as well as to achieve a more detailed examination of the melting region and the impact of the fluid

migration scheme without the consequences of iterative particle-to-node interpolation steps, we add a supplemental modeling step of one-dimensional calculation columns through the mantle wedge for the NIB and CCR models (Fig. 1). Columns originate at the slab-mantle interface immediately above the locations of fluid release, rise through the mantle wedge thermal field, and end where the activity of water in the peridotite drops below unity. If the result of a calculation is water-saturation, the excess fluid moves on to the next step (pressure-temperature point). The endpoint corresponds to water under-saturation due to preferential partitioning of water into the melt phase. The columns mimic the dimensional set-up of the GyPSM-S model in that steps between the vertically rising fluid and the wedge peridotite occur in intervals of 2 km along the vertical axis and the pressure and temperature of these equilibration steps are mapped directly from GyPSM-S output on the Eulerian mesh.

At the start of the model, the steps along the column have the same bulk composition [44] (Table 1). Prior source depletion due to melting at a back-arc or along a decompression trajectory associated with the solid flow field, is neglected. The columns begin water-saturated up to the respective solidus, which allows the fluid to arrive at the location of melting with negligible loss (loss may be due to stabilization of additional water in NAM as the material advects from lower to higher pressures, due to the increasing solubility of water in NAM with pressure). The first calculation involves the column associated with the lowest pressure fluid release. If melting is present, the bulk composition at that step along the column is then depleted. This depletion is carried along the flow field to the next column calculation, whereby the residues from the first column calculation become the starting compositions for the second column calculation and so on,

assuming advection of the solid down slab-parallel trajectories (Fig. 1a). Calculations to test for melting are performed by individual isothermal, isobaric pHMELTS equilibrations using the `adiabat_1ph` user interface [28]. We do not account for changes to the overall GyPSM-S-calculated temperature structure due to hydration or melting within the columns.

We consider fluid migration through the near-slab wedge in two ways: (i) using a fundamental assumption that at each interval fluid is fully equilibrated with mantle material (similar to the GyPSM-S calculation) and (ii) incorporating an assumption that fluids do not equilibrate with the already hydrated peridotite at each step, but carry the original fluid-mobile trace element composition with them until they reach a point at which melting begins. The difference in these two schemes is manifested within the fluid-mobile trace elements only, and represents two end-member possibilities for fluid transport within the near-slab region. For the full-equilibration sequence, if the column calculation is not the initial (lowest-pressure), the fluid-modified trace element composition of the peridotite from the previous column is used as a starting point to equilibrate with the fluid moving along the current column. For the isolated fluid transport case, the fluid retains its original trace element composition (a function of slab source lithology and initial fluid mass release) until reaching a zone of potential melting. At this point, the fluid-mobile trace element composition is added to the bulk peridotite composition which is then equilibrated by pHMELTS. If a calculation results in a very low-degree melt and water-saturation, the excess fluid mass is moved to the next column, assuming that the fluid trace element composition is preserved, but the amount of water able to move has decreased.

### *3.3. Slab dehydration and fluid release*

Within the context of GyPSM-S, compositionally-tagged Lagrangian particles within the slab carry lithological information and are the fluid sources in the model (Chapter 2). As the slab descends, the particles advect to higher pressures and temperatures, crossing univariant phase boundaries and dehydrating to produce a hydrous fluid, effectively acting as point sources. The dehydration reactions are controlled by the MORB and harzburgite phase diagrams of [45] (Fig. 2). We assume a hydration depth into the slab of 12 km, including 7 km of altered oceanic crust (AOC), and 5 km of fully-serpentinized mantle lithosphere. The serpentinization process is hypothesized to occur at the outer rise of subduction zones, where ocean water has the potential to penetrate down large normal faults into the mantle lithosphere, reacting with the lithospheric peridotite to produce hydrous phases such as antigorite and chrysotile [46]. Seismic surveys show the potential for hydration along lithospheric faults to up to 10 km depth [46], however, little is known about the average degree of serpentinization. We do not include sediments within this model, assuming that they dewater significantly by 50 km depth [16]. For the column models, we assume that dehydration of a particle within a slab element is representative of the total volume of that element such that the fluid mass released upon crossing a phase boundary (1.0 to 8.6 wt. % H<sub>2</sub>O) represents the effective fluid mass released into the first volume of wedge peridotite at the slab-mantle interface (the start of the column calculation). This is a maximum fluid flux, compared to the values resulting from the GyPSM-S calculation, and results in a maximum melt fraction.

#### *3.4. Trace element composition of migrating hydrous fluids (Table 2)*

The missing part of the puzzle is the addition of fluid-mobile trace elements, as pHMELTS is sufficient for calculating melt/residue trace element partitioning (including H<sub>2</sub>O). Forward modeling allows the generation of fluid-mobile trace element contributions from the AOC and the lithospheric serpentinite using published partition coefficients, initial concentrations, and the batch melting equation. Of course, the quality of the partition coefficient dataset limits the precision of the models, and the partition coefficients are assumed to remain constant for the respective bulk lithologies over a range of temperatures and pressures, and bulk compositions. We calculate the initial trace element content of the fluid for specific fluid-mobile tracers (Ba, Th, U, Pb, and Sr) based on equilibration of a mass of fluid (the release mass described above) with the slab source lithology using the following mass balance equation for each element:

$$\frac{C_{fluid}}{C_{initial}} = \frac{1}{D(1-F) + F} \quad , \quad (1)$$

where  $C_{fluid}$  is the concentration of a tracer in the fluid,  $C_{initial}$  is the concentration of a tracer in the bulk starting material,  $D$  is the rock/fluid partition coefficient, and  $F$  is the fluid fraction expressed as a weight percent. We used rock/fluid partition coefficients for fluid in equilibrium with eclogite ( $D^{eclogite/fluid}$ ) from Brenan et al. [47] and for fluid in equilibrium with serpentinite ( $D^{serpentinite/fluid}$ ) from Tenthorey and Hermann [48]. The values for  $D^{eclogite/fluid}$  were calculated assuming a 60:40 garnet:clinopyroxene assemblage. The source chemistry for eclogite is from the altered oceanic crust composition from McCulloch and Gamble [49]. The source chemistry for the serpentinite lithology is the serpentinitized

peridotite ETF1 (antigorite + olivine + diopside + chlorite + magnetite + Ti-clinohümite) from Erro-Tobbio, Western Alps, NW Italy, analyzed by Scambelluri et al. [50]. Notably, the lithospheric serpentinite composition, compared with the eclogite, is relatively depleted in LILE (Table 2).

For the fully-equilibrated scheme, in each subsequent subsolidus step, we equilibrate the fluid-mobile tracers with a peridotite source lithology based on partition coefficients for fluid in equilibrium with lherzolite ( $D^{\text{lherzolite/fluid}}$ ) [47], assuming 60:30:10 by mass olivine:orthopyroxene:clinopyroxene. The peridotite compositions are carried down from previous columns as described earlier. Errors may be introduced due to the changing bulk composition of the peridotite as it melts and is advected, especially as some melting steps lead to cpx-exhaustion. The resultant fluid-mobile contents from the fluid (including water as a trace element) are added to the bulk trace element composition of the peridotite prior to a pHMELTS equilibration, relative to the mass proportion of fluid added. After the calculation, any excess water is then given a fluid-mobile trace element content based on its mass fraction and is moved along to the next pressure-temperature point (see Notes to Table 2). Melts calculated by pHMELTS at the top of the column thus include the fluid-mobile trace elements added by the hydrous fluid phase. In the isolated transport case for fluid, the fluid interacts with the peridotite source lithology at the top of the column only, such that the resultant fluid-mobile elements are added to the bulk trace element composition of the peridotite prior to a pHMELTS equilibration, relative to the mass proportion of fluid added. Within the GyPSM-S model, fluid is transported using Darcy flow. For these simple models, we necessarily impose that fluid moves fast enough such that it will reach the top of the calculation column before advection of the solid would

move the column to new P-T conditions.

### *3.5. Melt transport*

The GyPSM-S calculation assumes a divergence-free, incompressible flow field and near-fractional melting, such that the melts are isolated immediately upon formation and have no further physical or chemical effect on the solid flow field. Realistic melt flow beneath subduction zones is most likely to be at least two-dimensional [23]; however, one-dimensional models can provide some insight. In the context of the columns introduced above, we examine the compositions of the melts as they are initiated and address the fate of melts initiated at different depths and distances into the wedge in the context of near-vertical buoyant transport towards the surface. Near-vertical transport allows for the least complicated manner of equating melts initiated at different depths to different locations in a cross-arc sense. Two end-member possibilities for melt-solid interaction along this type of trajectory are evaluated.

The fate of the melt can theoretically fit into one of two categories: (i) chemically isolated transport (perhaps along unreactive channels, or along fractures) and (ii) reactive transport (porous flow). Both scenarios can be addressed within the column configuration. During the original calculation, described above, information as to the pressure, temperature, composition, and mass fraction of melts generated along a column is provided. However, the original column assumes the transport of water in a hydrous fluid only, and the calculation ends when the activity of water drops below unity. The melting calculation employs an extension of the original column, further mapping pressures and

temperatures at each point from the GyPSM-S mesh. A single initial melt composition from each original column, representing the maximum melt fraction experienced for that column, is extracted. In the case of chemically isolated transport, we examine the situation in which these melts continue to travel along their respective column extensions in chemical isolation from the surrounding peridotite (scaling the melt mass to 100.0 g of material). If a calculation results in the persistence of the melt phase, the melt is extracted and moved to the next point along the column extension. This is a case of closed system transport, where there is no exchange of mass. In the case of reactive transport, we examine an open system in which the melt continues to move along the column, but with complete equilibration with the surrounding peridotite at each step. In both cases, there is complete physical separation of the melt and residue after each step, such that it is the melt phase alone that moves up the column. For both cases, the extended column calculation continues until the melt fraction drops to zero or the limits of pHMELTS stability are reached.

## **4. Results**

### *4.1. Dehydration patterns as a function of subduction parameters*

Due to the specification of vertical fluid transport through the mantle wedge, the locations of melt initiation are controlled by the positions of the dehydration reactions within the different lithologic layers within the slab [45]. These reactions generate different dehydration patterns in different models due to the changing thermal structure of

the model slabs. In all models, there appears to be a roughly bimodal distribution of fluid sources and an overall evolution in the host reservoir with distance along the slab (Fig. 3). In subduction zones defined by a younger slab, the AOC layer and the serpentinite layer completely dehydrate by the time they exit the base of the model domain (200 km). The AOC layer dehydrates over a pressure range of  $\sim 1$  GPa before 100 km depth. The serpentinite layer dehydrates in a series of reactions starting  $\sim 3$  GPa and ending  $\sim 6$  GPa (rock containing serpentinite chlorite brucite  $\rightarrow$  serpentinite chlorite dunite; serpentinite chlorite dunite  $\rightarrow$  chlorite harzburgite; chlorite harzburgite  $\rightarrow$  garnet harzburgite; Fig. 2; lithologic descriptions from [45]). In models defined by subduction of a more mature slab, the AOC layer dehydrates over a longer pressure range ( $\sim 2$  GPa) extending to greater depths. The serpentinite layer crosses a single phase boundary and exits the model domain with 6.8 wt. % H<sub>2</sub>O. Increasing the downgoing slab thermal age results in a very strong fluid source from the serpentinite layer at higher pressures ( $\geq 5.9$  GPa), as opposed to a relatively weak fluid source from the serpentinite layer associated with younger slabs at lower pressures. This is due to the change in the thermal structure of the slab, resulting in altering the P-T trajectory across phase boundaries (Fig. 2).

The primary effect of increasing slab velocity at a similar convergence angle is a relative deepening of the serpentinite reactions, as a faster slab leads to an overall cooler thermal structure. Changing the convergence angle does not seem to impact the fluid release pattern with depth, but does have a significant impact on the horizontal (arc-normal) expanse of the melting region [39]. Increasing slab dip ( $45^\circ$  to  $60^\circ$ ) allows the strong serpentinite-derived fluid source to approach the melting region associated with AOC-derived fluid sources. Decreasing slab dip ( $45^\circ$  to  $30^\circ$ ) increases the horizontal extent of

the melting region, distributing fluids over a wider interval (Fig. 3e, f). This has a primary influence on the ultimate geometry of the hydrated region within the wedge.

We have modeled the dehydration of both AOC and serpentinite as point sources associated with crossing of sharp univariant boundaries, but recognize that in reality the AOC at least is likely to experience more continuous dehydration associated with reactions of higher variance. Serpentinite, being a relatively simple compositional system with more limited solid solution, is expected to behave in a manner closer to the point source approximation. The fluid flux from the slab increases with depth for the models with older slabs as a function of the capacity of the deeper-dehydrating serpentinite minerals and the position of the phase boundary. For younger slab models this is not the case, and the majority of the fluid is released from the interval  $\sim 2.5$ - $3.5$  GPa. Mid-pressure fluid release ( $< 4.0$  GPa) from younger slabs is primarily a product of the serpentinite layer, while for more mature slabs it is the AOC layer.

Especially in the case of the younger slabs, very shallow fluid release results in the hydration of the peridotite wedge without melting, and the fluid continues to migrate up into the overlying lithosphere. Shallow fluid release into the near-slab mantle immediately adjacent to the wedge corner is all that is necessary to initiate the LVC, as the thermal structure inhibits release of water from the NAM along slab-parallel streamlines.

#### *4.2. Time-dependent consequences of dehydration patterns*

Based on GyPSM-S results (Chapter 2), the deepest serpentinite-derived fluid sources from mature slabs lead to a strong continuous flux to the deeper melt region. As a

result of the latent heat of melting, significant continuous cooling of the active melting region can occur, and the position of the water-saturated solidus may ultimately retreat into the wedge, producing a longer fluid pathway leading to shallower melting associated with the serpentinite fluid source. This mechanism is a way to generate hydrous melts derived from deep slab fluid sources at relatively low pressures. Younger slabs do not exhibit this behavior, primarily due to the lack of a similar strong fluid source at depth. Instead, models with younger slabs maintain the uniform-thickness channel configuration throughout the model duration.

#### *4.3. Melt characteristics*

The positions and relative strengths of the fluid sources are important for the fluid-mobile trace element chemistry of the resulting melts. As shown in Table 2, the fluid-mobile trace element compositions of the fluids derived from the lithospheric serpentinite are more depleted than those originating from the AOC layer, resulting in different melt trace element signatures depending on the direct fluid source to a specific melting region. Thus, the serpentinite provides a significantly greater fluid source without a corresponding increase in fluid-mobile components (Fig. 4) [15]. There is a strong control on the initiation of melting with the influx of fluid, and all initial melts are very hydrous, with 8-15 wt.% H<sub>2</sub>O (higher pressure initial melts have less water). There is not a simple pressure-dependent trend of instantaneous melt fraction ( $f$ ) of the initial melts that appear in the system. Single columns can produce multiple degrees of  $f$ , and in some cases, particularly at shallower melting regions, multiple melts with significantly different

concentrations of indicators of source depletion, such as HFSE, and significantly different major element compositions.

The cumulative melt fraction ( $F$ ) experienced by a packet of mantle within the calculation column as it moves past the base of the model domain (Fig. 5) changes dramatically between the model with the younger slab and the model with the more mature slab. Larger fluid flux from the mid-pressure serpentinite fluid releases within the younger slab result in very high  $F$  ( $> 35$  wt. %) in the center of the column. Higher fluid flux leads to higher extents of melting for mid-pressure melts. For the mature slab case, the maximum  $F$  experienced at mid-pressures is  $\sim 20$  wt. %, with a significant tail (up to 10 wt. %) appearing at higher pressures, extending further into the wedge. This is due to the relatively lesser fluid mass released from the mid-pressure AOC layers for this model case. In all cases, the activity of water rapidly drops below unity as the water is partitioned into the melt phase (Fig. 6). Restricting water transport to a hydrous fluid phase results in a sharp boundary in the water content of NAM and in solid density ( $\Delta\rho \sim 20\text{-}50$  kg/m<sup>3</sup>) between the LVC and the ambient mantle above the melting region. These density contrasts are not enough to initiate Rayleigh-Taylor instabilities leading to diapirism of the hydrated solid (e.g. [52]); however, the water content boundary leads to strong lateral variations in solid viscosity which have an impact on the flow field as well as geophysical surface observables (Chapter 4).

#### *4.4. Changing bulk composition-melt depletion patterns within the wedge flow field*

A combination of changing bulk composition due to melting along previous

columns, and of the gradual divergence of the pressure-temperature path of the slab surface from the water-saturated solidus, causes the active melting region to occur as a thin lens that appears at a greater distance from the slab interface with increasing depth. In most cases, material is not being progressively depleted by melting, but rather fluid migration occurs through previously melt-depleted regions to less-depleted (or non-depleted) sources towards the interior of the wedge. Therefore, there is an overall combination of melts produced from fertile sources and melts produced from depleted sources. Melts associated with deeper fluid releases are uniformly from more fertile sources.

In real subduction systems, there is the potential for sequential melting of mantle peridotite as it advects along streamlines within the wedge, including upwelling beneath a back-arc, melting beneath rear-arc volcanoes, and then beneath the magmatic front itself [15, 19, 49, 64]. However, in this study, previous depletions due to such factors are neglected, and depletion trends in the trace elements can be seen solely as a consequence of proximity of fluid sources in the low- to mid-pressure regions, leading to certain cases of additional fluxing of material previously depleted by melting. This is particularly appropriate for the NIB system, which has very depleted arc lavas, yet no active back-arc spreading [33]. As demonstrated by the results presented here, and as suggested by [68], hydrous fluxing alone may maintain the depletion of arc sources. Even if the presence of a back-arc is considered, the solid flow pattern is such that more wedge-interior streamlines may not have passed through melting regions feeding the back-arc melting region, leading to a general trend of melts from less depleted sources associated with deeper fluid releases (Fig. 7). This leads to an apparent paradox: the most fertile sources receive the most depleted fluids.

#### 4.5. Melt chemistry

Incompatible element ratios that reflect source depletion vary with spatial location within the wedge and are not significantly affected by the method in which fluids transit the hydrated region. These ratios show a bimodal distribution correlated with pressure of initial melting. For example, Zr/Nb increases with source depletion [15], and the highest values are found in low- to mid-pressure melting regions (Fig. 8a), influenced by more closely-spaced fluid sources. Melts become more depleted with pressure, as residues from previous melting events are advected down-dip and additionally melt. However, these melts are generally low melt fraction, and do not result in water-undersaturation. Fluids tend to continue to move through to fertile sources immediately above the depleted sources, resulting in additional melting with significantly higher melt fractions in the same column. The residues from the low- to mid-pressure melting region do not influence the deepest melts, and as such the deep source region is less depleted overall. Thus, Zr/Nb decreases with increasing pressure of melting overall. Nb/Yb decreases as the mantle source becomes more depleted [53] (Fig. 8b) and increases with pressure of melting, overall. These model data imply that the most depleted melts are associated with low- to mid-pressure fluid sources: the AOC (eclogite) layer in the case of mature slabs and the serpentinized lithosphere in the case of younger slabs.

Geochemical tracers carried with slab-derived fluids are affected by the mechanism of fluid transport (fully-equilibrated or isolated) through the hydrated near-slab wedge. Ba shows the most dramatic difference, as its concentration in the fully-equilibrated case

rapidly increases within the LVC (a consequence of the low  $D^{\text{herzolite/fluid}}$  for Ba and of the fluid carrying more Ba due to consecutive equilibration with a peridotite composition carrying more Ba). Indeed, concentrations of Ba in the peridotite become unrealistic in the fully-equilibrated fluid transport end-member. In contrast, the method of isolated transport of the fluid, with interaction only at the top of the column, results in trace element ratios within the range of regional datasets. The fully-equilibrated fluid path results in slight enrichments of Pb in the initial melts at all pressures and U and Sr at low- to mid-pressures relative to the limited interaction fluid path. Th contents in the initial melts are not significantly affected by the choice of fluid transport scheme.

Plots of Zr/Nb vs. U/Th (Fig. 8d, e) show the depletion trends together with the degree of hydration. Higher U/Th is expected for mantle sources metasomatized by hydrous fluids, whereas higher Zr/Nb is expected for depleted mantle sources, as mentioned previously. Values for the melts associated with young slab serpentinite fluid release and mature slab AOC fluid release appear to most closely match the real datasets, potentially indicating that the regions of highest melt production (mid-pressure) are most readily represented at the arc front, and that changing subduction parameters result in changing fluid source lithology responsible for the mid-pressure fluid release .

The La/Yb ratio represents the mantle source's enrichment in incompatible elements, generally relating to the amount of melting [15, 16], and the Ba/La ratio represents the slab-derived fluid's contribution, or the relative slab signal [16]. Plots of La/Yb vs. Ba/La (Fig. 8f, g) show that in both models, melts influenced by AOC-derived fluids have lower La/Yb and higher Ba/La. The model melts influenced by serpentinite-derived fluids are closer fitting to the dataset for Costa Rica, while the model melts

influenced by AOC-derived fluids are closer fitting to the Izu-Bonin dataset. It should be noted that the Carr dataset [55] for Costa Rica has anomalously high values for La/Yb, derived from Galapagos-like mantle in the area [42, 56].

Some ratios of fluid-mobile incompatible elements to HFSE (generally assumed not to be mobile in fluids), such as Ba/Nb, can be indicative of the total subduction component that is added to the arc magma source [53] (Fig. 9). Ba/Nb ratios in these models range from  $> 200.0$ - $2100.0$  for lower pressure melts to  $< 200.0$ - $600.0$  for higher pressure melts. These values are all much higher than for N-MORB (Ba/Nb  $\sim 4$ ), reflecting the influence of the slab-related fluid sources [54]. For the NIB model, Ba/Nb decreases with increasing pressure. Plots of Ba/Th and U/Th (Fig. 9c, d) comparing the Carr dataset with model melts show that the serpentinite-derived fluids from CCR more closely match the data from Costa Rica.

The major element composition of the initial melts are shown in Table 4. The initial melts are very hydrous, as mentioned previously. Overall, initial melts at low- to mid-pressures have higher SiO<sub>2</sub>, Al<sub>2</sub>O<sub>3</sub>, and H<sub>2</sub>O and lower TiO<sub>2</sub> contents than higher pressure melts. Na<sub>2</sub>O varies primarily by melt fraction.

#### *4.6. Simple models for melt extraction*

We attempt two column-based tests of melt extraction: full equilibration of the melt along the column pressure-temperature conditions, and isolated transport of the melt along the column pressure-temperature conditions. When melt is fully equilibrated with ambient peridotite at each additional step along the column, two trends emerge (Fig. 10). For initial

melts that have formed at relatively shallow depths, equilibration up the column results in the progressive dehydration of resultant melts and increasing activity of water in the system, with concurrent increases in the water content of NAM along the column. Ultimately, around 1.35 GPa, hornblende is added to the assemblage. The additional column calculation ends with the activity of water reaching unity (second boiling) and melting ceasing around 1.15 GPa. There is a very abrupt contrast between the conditions at the top of this column and the ambient conditions in terms of water activity and solid density ( $a_{H_2O} = 1.0$  versus 0.3;  $\rho_{solids} = 3.16$  versus 3.28 g/cm<sup>3</sup>). For initial melts that have formed at higher pressures, the column extension is much longer, yet involves much lower melt fractions. Hornblende stability is never reached, due to the higher pressures. Instead, water is progressively partitioned into the NAM, with water activity and solid density decreasing to ambient levels ( $a_{H_2O} = 0.08$ ;  $\rho_{solids} = 3.27$  g/cm<sup>3</sup>). Interestingly, the situation of complete melt equilibration along a path results in an extension of the hydrated layer beyond the original thickness of the LVC. For the case of isolated transport of melt along the pressure-temperature path specified by an extension of the original column, second boiling occurs at relatively greater depths (~1.25 GPa).

For a test of directly matching the model-derived initial melt compositions with real lava chemistry from the northern Izu-Bonin system, we attempted a "direct-delivery" model. We calculated a primary magma composition for a local volcano (Miyakejima, Table 5) based on fractionation pathways that matched analyzed lava compositions [72] under conditions of isobaric cooling in a hypothetical magma chamber at 500 bars, with  $f_o = \text{QFM}+0.5$  (Fig. 11). We find that none of the individual modeled NIB melt compositions

provided a match for the calculated Miyakejima primary magma composition. Indeed, neither did a direct combination of the modeled NIB melts as investigated by a singular value decomposition (SVD) analysis. However, this is an extremely idealized approach, assuming no melt-residue interaction and the result is not surprising.

## **5. Discussion**

### *5.1. Fluid transport within the LVC and potential consequences of a lack of sediment*

Fluid transport modeling with the assumption of full equilibration of the fluid with peridotite along the entire thickness of the LVC is not matched by the fluid-mobile trace element datasets for either region. In fact, it is the assumption of equilibration of the fluid with peridotite only at the top of the transport pathway that appears to be more valid. These end-member results could be indicative of limited interaction of the fluids with the hydrated peridotite along the pathway, not necessarily only near the melting region. As the LVC is initiated near the wedge corner, at the shallowest locations of fluid release, and water in NAM is quite stable within the LVC throughout its transit to (at least) the base of the model domain (200 km depth), the primary impact of the equilibration of fluid is to increase the water content, and perhaps thicken the LVC. A more limited interaction will not negate the presence or persistence of the LVC, and will act to more readily preserve the differences in fluid-mobile trace element chemistry derived from particular source lithologies along the slab, leading to discernible influences on the initial melt chemistry that vary spatially within the wedge. If these differences are preserved, and a melt

migration scheme acts to prevent significant mixing of magmas within the wedge, such that melts associated with higher-pressure-derived slab fluids will erupt separately from melts associated with lower-pressure-derived slab fluids, cross-arc variations in lava trace element chemistry become significant for depth tracing of initial melts.

The concept of a changing fluid-source slab lithology manifested in rear-arc to arc geochemical trajectories has been proposed by previous studies [15, 19]. The Guguan cross-arc chain represents the fluid-fluxed end-member of the intraoceanic Mariana arc and involves subduction of a mature slab [9, 63]. Stern et al. [15] propose that changing slab sources of metasomatic fluids with depth lead to variations in the fluid-mobile trace element concentrations in the lavas in this system (Fig. 7), concluding that there may be an increasing role of serpentinite-derived fluids at greater depths leading to rear-arc volcanism due to the appearance of a weakening slab signature with increasing distance to the WBZ. As hypothesized by [15], this could simply be due to the relative lack of LILE in subducting serpentinitized lithosphere. Notably, the water contents of rear-arc lavas are not shown to change markedly from volcanic front lavas, further suggesting a changing slab fluid source to serpentinite, which provides a significant fluid flux [15]. If the fluid source-derived geochemical differences are preserved, changing subduction parameters (such as slab dip) may produce changing lava geochemistry, as different fluid sources are emphasized. For example, volcanic front lavas along the Central American subduction system demonstrate that trace element data may preserve information about the relative influences of fluid-source lithology as ratios associated with a slab signal vary with respect to changing subduction parameters [16].

This study neglects sediment-derived fluid contributions to the fluid budget, as well

as sediment melts, or melts of the AOC [57]. We assume that sediment-derived fluids are expelled at shallower depths than the convecting mantle wedge [16], but the lack of sediment melting may be significant. At present, modeling of slab-derived components encompasses selected fluid-mobile trace elements only. Melting of sediment allows for the bulk addition of elements concentrated in the sediment layer to the mantle wedge that may not be effectively added through fluid-dominated transport alone, due to the very low mobility of certain elements within a fluid. These elements include the HFSE (Nb, Ta, Zr, and Hf), REE, and possibly Th [9, 47, 58]. Neglecting sediment melting effectively results in the potential for higher concentrations of these elements than predicted by this study.

## *5.2. Comparison of model results with regional datasets*

### *5.2.1 Costa Rica (CCR)*

Rupke et al. [16] use a 2-D dynamic model to track the evolving sources of fluid release from the downgoing slab in the Costa Rican subduction zone. The results show that sediments dewater by 75% during shallow (< 50 km) subduction, the AOC (the most significant source of the slab-derived fluid flux) dewateres over an interval 100-140 km depth, and serpentinites dewater over an interval 130-150 km depth. Our results show a similar overlap between AOC and serpentinite dehydration, but that serpentinite is the major source of mid-pressure (80-130 km depth) fluid flux. Significantly, the fluid sources for the CCR model in this study and the model of [16], despite the fundamental difference in fluid-source lithology, feed into similar spatial melting regions. These mid-pressure

melts represent the result of the highest fluid flux in the CCR model, as well as the highest melt fraction, and can thus be considered to be the primary input towards the volcanic front. Lithospheric serpentinite is relatively depleted in fluid-mobile elements compared to subducting AOC. The reason the concentration of trace elements added to the melting region from the dehydrating slab decreases beneath Costa Rica as opposed to neighboring regions with different subduction parameters [16, 39, 42, 43] may be this change in fluid source lithology. The range of melting expected beneath Costa Rica is 5-25% [39], which is significantly lower than the maximum degree of melting produced by the column modeling of this study, but is not inconsistent with the overall range of melting produced by the columns (Fig. 5). The upper value is probably a consequence of a maximum fluid flux to the active melting region in the column modeling.

Carr et al. [59] argues that regional along-arc variation in Ba/La in the Central American subduction system is a result of the manner of fluid delivery and its impact on melt production. Specifically, Carr et al. [59] contends that the steeper-dipping, slightly older slab beneath the Nicaraguan segment involves more concentrated fluid delivery, leading to higher Ba/La, while more diffuse fluid introduction in Costa Rica, a function of the more moderately-dipping slab, leads to lower Ba/La ratios. Modeling of a steeper-dipping slab by GyPSM-S agrees with the potential for a more concentrated fluid flux to mid-pressure regions feeding the volcanic front as fluids from depth transit pathways approaching the same melting region as influenced by shallower fluid release. However, an additional factor for consideration may be the fluid-source lithology. Fluids derived from the slab AOC layer tend to result in melts with higher Ba/La ratios, while fluids derived from the slab serpentinitized lithospheric layer tend to result in melts with lower

Ba/La. Perhaps there is a change from mid-pressure AOC-derived fluid flux under Nicaragua to mid-pressure serpentinite-derived flux beneath Costa Rica, a function of the slightly different slab age. This would not preclude the arguments of [37], which lead to the conclusion that there is a strong slab-derived fluid source designated by a low- $\delta^{18}\text{O}$  water-rich component beneath Nicaragua. We suggest that it is the deeper AOC layers that would be dehydrating at the mid-pressure ranges, and hydrothermally-altered lower oceanic crust and hydrothermally-altered ultramafic rocks both have similar ranges for oxygen isotope values ( $\delta^{18}\text{O}_{\text{SMOW}} = 0\text{-}6\text{‰}$ ) [60-62].

### 5.2.2 *Izu-Bonin*

Izu-Bonin arc tephra geochemistry indicates minimal contribution from subducted sediment, a dominantly fluid-based slab component transport scheme, and a highly depleted mantle source for the volcanic arc [32]. Additionally, there is a cross-arc distribution of chemical characteristics that indicates that the melt transport systematics can be described relatively simply [19] and shows evidence for a lack of crustal contamination [31]. We propose that there is a maximum contribution at the volcanic front from primary magmas fluxed by mid-pressure fluid release from dehydrating slab AOC layers and that rear-arc lavas (Western Seamounts) involve significant contributions from primary magmas fluxed by fluids released at higher pressures from the dehydrating slab serpentinite layer.

Hochstaedter et al. [19] note significant cross-arc trends for the Izu-Bonin system, including increasing Nb/Zr (decreasing mantle source depletion) and decreasing Ba/Nb and  $\text{SiO}_2$  with distance from the volcanic front to the rear-arc. These trends agree with the

results of this study, assuming a melt migration pathway allowing melts initiated by fluids released lower pressures to influence the volcanic front, and melts initiated by fluids released at higher pressure to influence the rear-arc. Specifically, with regard to the end-member results for limited fluid interaction, the values for Ba/Nb for the low- to mid-pressure melts and the higher-pressure melts match very closely the data from [19], for volcanic front lavas and rear-arc lavas, respectively (Fig. 9b). Additionally, we observe a trend of decreasing  $\text{SiO}_2$  with increasing pressure among initial modeled melts, and trace element indicators of mantle source depletion show that melts associated with low- to mid-pressures are the most depleted in HFSE, a pattern that matches the data from [19] indicating that the volcanic front lavas are the most depleted of the arc system (Fig. 8). Stern et al. [15] additionally observe increasing mantle source depletion with decreasing distance to the WBZ.

Hochstaedter et al. [19] propose that a mechanism of fluid depletion can explain the cross-arc variation, such that a "fertile" (higher in fluid-mobile elements) fluid is released at lower pressures, and a then more "depleted" fluid (a result of the earlier fluid release) is released at higher pressures. We suggest that instead of a progressively-dehydrating singular slab-source that evolves with regard to concentrations of fluid-mobile elements, there is a condition of progressive dehydration from heterogeneous slab lithologies defined by different initial fluid-mobile trace element compositions and varying fluid fluxes, a situation similar to that modeled by [16] and suggested by [15].

GyPSM-S results for the subduction of a mature slab indicate that there is a time-dependent evolution of the hydrated low-viscosity region from a channel into a more extensive wedge-type geometry (Chapter 2). This is a consequence of the strong, deep

serpentinite-derived fluid flux in mature slabs and the effect of the latent heat of melting. Progressive cooling associated with the active melting region may eventually lead to the retreat of the solidus into the wedge and a lengthening of the deeply originating fluid pathway over time. This should not effect the overall trace element chemistry of the low- to mid-pressure melts presented in this study. For the melts influenced by the deeply-derived fluid source, the lower degree of prior depletion relative to certain melts derived from low- to mid-pressure fluid releases should remain the same, and if the hypothesis of limited interaction with the wedge peridotite is correct, the fluid-mobile trace element composition of these melts should remain consistent with the results presented here.

### *5.3. End-member results for vertical melt transport*

We find a close spatial agreement with the GyPSM-S modeled locations of melt initiation and seismic imaging results for low-velocity zones within the wedge [2, 3, 66], indicating that models of the active melting region are successful. However, in order to preserve the spatial heterogeneity of initial melts as described in previous studies of cross-arc geochemistry, a nearly-vertical melt migration model is required. This model should readily allow the arrival of melts fluxed by fluids derived from lower pressures towards the arc front versus melts fluxed by fluids derived from higher pressures towards the rear-arc. The rear-arc lavas in the Guguan chain show higher pressures and temperature of equilibration [15], an indication that deeper melts may tend to influence volcanism towards the rear of the arc as opposed to the volcanic front itself. There also appear to be lower degrees of melting experienced as depth to the WBZ increases in the Guguan chain (shown

from variations in alkali content [15]), a similar result to the column modeling, where deeper melting of less depleted sources results in lower melt fractions (Fig. 5).

This study involves the investigation of two end-member interaction scenarios involving the implications of vertical melt transport originating at the zone of active melting and continuing through the mantle wedge. A scenario in which melts remain isolated from the surrounding peridotite matrix results in a short additional transit of the melt before it results in second boiling. In the case of an "infinitely permeable" scenario defined by batch melting, melt migrates along vertical paths, with a full equilibration with ambient peridotite at each step. The possibility of high water contents in NAM is extended further from the slab into the wedge, providing a potential mechanism to generate a more extensive low-viscosity geometry. Melts continue to react along the column to the point of freezing out (higher-P) or stabilizing hornblende (lower-P). Because melts have to approach the surface in order to result in arc lavas, an infinitely permeable scenario can only work for part of the transport process (< 40 km depth), and only for shallower melts. The deepest melts in the models may end up as source enriching agents rather than coherent melts passing through the long potential melting column to eruption. In both end-member cases, the column calculation ends well before the depth of potential shallow magma chambers feeding the arc, resulting in the conclusion that neither of these interaction mechanisms by itself defines the entire melt extraction pathway.

#### *5.4. Implications for slab-component transport rates*

The stability of the slab-adjacent hydrated zone (LVC) and the separation of the

slab-wedge interface from the melting region has been established through GyPSM-S. Studies of slab-fluid component transport to the arc using U-series isotopes indicate a timeframe of transport from fluid release to eruption between 30,000 and 120,000 years, allowing for a fluid transport rate of 1-4 m/yr [14], and implying the probability of a rapid transport pathway. Current GyPSM-S parameters for fluid transport allow for 0.63 m/yr as a fluid velocity, on the lower end of that estimate. From comparison with regional datasets, the results presented in this study indicate that fluids responsible for flux melting may preserve the trace element signatures of the original dehydrating lithology with little modification along their pathway through the LVC to the melting region. This suggests either a potential rapid transport scenario that prevents significant fluid-mantle interaction or a fluid-dominated trace element budget. Perhaps hydraulic fracture plays a subordinate role in the slab-adjacent mantle wedge, allowing for a more or less direct delivery of fluid to melting region [65].

##### *5.5. Implications for back-arc basin basalt (BABB) sources*

There is a critical role of water, originating presumably at the slab-wedge interface, evident in the petrogenesis of basalts erupted at back-arc basins [67-69]. However, the pathways of water delivery from the slab to the back-arc melting region have not been clearly established. In this study, we do not include a back-arc spreading region and cannot therefore offer a unique solution. Despite this, we can infer potential hydrous pathways leading to melting beneath the back-arc from the results presented here.

### *5.5.1 Direct delivery of fluids to the shallow-level wedge*

Previous investigation of BABB geochemistry invokes mixing between dry, fractional melts and hydrous melts that have been equilibrated at low pressures [51]. The hydrous end-member is associated with fluid influx from the slab, and requires low-pressure equilibration in order to explain aspects of the geochemistry of BABBs such as low  $\text{Fe}_{8.0}$  and the lack of a garnet signature [51].

The model domain in GyPSM-S extends to 200 km depth, and dehydration reactions within the slab over that depth range lead to active melting that can explain trace element variations evident in cross-arc lavas. Rupke et al. [70] hypothesize that serpentinite dehydration reactions within the slab, and possibly within the hydrated near-slab mantle, can occur at even greater depths, allowing for melting to initiate further inboard from the arc, perhaps extending beneath a back-arc. Deeper sources may eventually translate into longer serpentinite-derived fluid pathways to shallower melting regions beneath the back-arc, similar to the mature slab GyPSM-S results (Chapter 2). This could potentially translate into low-pressure hydrous melting beneath the back-arc as required by [51] (Fig. 12a).

### *5.5.2 Diapirism*

Even if fluid pathways did not reach directly into the BABB source region, fluids generated by deep serpentinite dehydration result in hydrous melting further into the mantle wedge than at shallower areas, removing the active melting region farther from the

down-dip influence of the slab-parallel solid flow field. The density differences between the initial melts and solid residue are significant ( $\Delta\rho = 400\text{-}500 \text{ kg/m}^3$ ), and could result in buoyant transport of hydrous melts as diapirs vertically into the BABB source region, as suggested by [51] (Fig. 12b).

### *5.5.3 Transport of enriched material along solid flow streamlines*

Porous flow of relatively low-degree melts at depth may result in an extension of wedge hydration above the zone of fluid delivery to the active melting region. The concentrations of water in NAM are increased in the solid residue due to equilibration with the migrating hydrous melt. Ultimately, the melt will freeze out in this process, but the remaining solid along its migration path may then be carried as hydrous enrichments with the flow field towards the back-arc source region (Fig. 12c).

## **6. Conclusions**

This study involves a supplement to original GyPSM-S modeling of systems with varying subduction parameters in order to demonstrate the applicability of GyPSM-S results to regional geochemical datasets. Changing patterns of fluid release from dehydration reactions within slab lithologic layers as a function of distance along the slab were investigated and related to the influence of changing parameters such as slab age and convergence velocity. Modeling of fluid migration through hydrated peridotite within the LVC provides evidence for a limited fluid-rock interaction, preserving the fluid-mobile

trace element chemistry associated with the original slab lithology to the active melting region. This suggests the potential for either a rapid fluid transport scenario or a fluid-dominated trace element budget within the LVC. Comparison with interpretations of along-arc trends suggests that changing subduction parameters significantly affect the dehydration pattern within the subducting slab, leading to changes in reaction location within the slab and a varying fluid flux and fluid chemistry reaching the active melting region, which can be manifested in erupted lavas. By comparison with regional datasets and interpretations of cross-arc and along-arc trends, we find that a simple melt migration scheme which preserves spatial heterogeneity of initial melts towards eruption is likely. Specifically, that melts associated with low- to mid-pressure fluid release will erupt towards the volcanic front and melts associated with higher-pressure fluid release will erupt towards the rear-arc. Although we do not explicitly include a back-arc in these models, interpretations of the results lead to several potential mechanisms to explain hydrous inputs to back-arc source regions.

### **Acknowledgments**

The authors would like to thank P. Antoshechkina and M. Gurnis for collaboration in the GyPSM-S modeling effort. Support provided through the Tectonics Observatory by the Gordon and Betty Moore Foundation.

### **References**

- [1] T. Plank and C. H. Langmuir (1988) An evaluation of the global variations in the major element chemistry of arc basalts. *Earth and Planetary Science Letters* **90**(4), 349-370.
- [2] A. Hasegawa et al. (2005) Deep structure of the northeastern Japan arc and its implications for crustal deformation and shallow seismic activity. *Tectonophysics* **403**, 59-75.
- [3] D. P. Zhao et al. (2001) Seismological structure of subduction zones and its implications for arc magmatism and dynamics. *Physics of the Earth and Planetary Interiors* **127**, 197-214.
- [4] G. A. Gaetani and T. L. Grove (1998) The influence of water on melting of mantle peridotite. *Contributions to Mineralogy and Petrology* **131**(4), 323-346.
- [5] G. A. Gaetani and T. L. Grove (2003) Experimental constraints on melt generation in the mantle wedge. *Geophysical Monograph* 138, 107-134.
- [6] E. M. Stolper (1980) A phase diagram for mid-ocean ridge basalts. *Contributions to Mineralogy and Petrology* **74**, 13-27.
- [7] E. M. Klein and C. H. Langmuir (1987) Global correlations of ocean ridge basalt chemistry with axial depth and crustal thickness. *Journal of Geophysical Research* **92**(B8), 8089-8115.
- [8] T. Plank and C. H. Langmuir (1993) Tracing trace elements from sediment input to volcanic output at subduction zones. *Nature* **362**, 739-743.
- [9] T. Elliott et al. (1997) Element transport from slab to volcanic front at the Mariana arc. *Journal of Geophysical Research* **102**(B7), 14991-15019.
- [10] T. Ishikawa and F. Tera (1999) Two isotopically distinct fluids fluid components

- involved in the Mariana Arc; evidence from Nb/B ratios and B, Sr, Nd, and Pb isotope systematics. *Geology* **27**, 83-86.
- [11] P. Ulmer and V. Trommsdorf (1995) Serpentine stability to mantle depths and subduction-related magmatism. *Science* **268**, 858-861.
- [12] M. W. Schmidt and S. Poli (1998) Experimentally based water budgets for dehydrating slabs and consequences for arc magma generation. *Earth and Planetary Science Letters* **163**, 361-379.
- [13] R. J. Arculus (1994) Aspects of magma genesis in arcs. *Lithos* **33**, 189-208.
- [14] C. Hawkesworth et al. (1997) U-Th isotopes in arc magmas: Implications for element transfer from the subducted crust. *Science* **276**, 551-555.
- [15] R. J. Stern et al. (2006) Subduction factory processes beneath the Guguan cross-chain, Mariana Arc: no role for sediments, are serpentinites important? *Contributions to Mineralogy and Petrology* **151**(2), 202-221, doi: 10.1007/s00410-005-0055-2.
- [16] L. H. Rupke et al. (2002) Are regional variations in Central American arc lavas due to differing basaltic versus peridotitic slab sources of fluids? *Geology* **30**(11), 1035-1038.
- [17] H. Iwamori (1998) Transportation of H<sub>2</sub>O and melting in subduction zones. *Earth and Planetary Science Letters* **160**, 65-80.
- [18] J. G. Ryan et al. (1995) Cross-arc geochemical variations in Kurile arc as a function of slab depth. *Science* **270**, 625-627.
- [19] A. Hochstaedter et al. (2001) Across-arc geochemical trends in the Izu-Bonin arc: contributions from the subducting slab. *Geochemistry, Geophysics, Geosystems*

2:2000GC000105.

- [20] P. D. Asimow, J. E. Dixon, C. H. Langmuir (2004) A hydrous melting and fractionation model for mid-ocean ridge basalts: Application to the Mid-Atlantic Ridge near the Azores. *Geochemistry, Geophysics, Geosystems* **5**(1), Q01E16, doi:10.1029/2003GC000568.
- [21] G. Hirth and D. L. Kohlstedt (1996) Water in the oceanic upper mantle; implications for rheology, melt extraction, and the evolution of the lithosphere. *Earth and Planetary Science Letters* **144**(1-2), 93-108.
- [22] J. H. Davies and D. J. Stevenson (1991) Physical model of source region of subduction zone volcanics. *Journal of Geophysical Research* **97**(B2), 2037-2070.
- [23] M. Spiegelman and D. McKenzie (1987) Simple 2-D models for melt extraction at mid-ocean ridges and island arcs. *Earth and Planetary Science Letters* **83**, 137-152.
- [24] P. Hall and C. Kincaid (2001) Diapiric flow at subduction zones: A recipe for rapid transport. *Science* **292**, 2472-2475.
- [25] F. Furukawa (1993) Magmatic processes under arcs and formation of the volcanic front. *Journal of Geophysical Research* **98**, 8309-8319.
- [26] P. B. Kelemen et al. (1997) A review of melt migration processes in the adiabatically upwelling mantle beneath oceanic spreading ridges. *Phil. Trans. R. Soc. Lond. A* **355**, 283-318.
- [27] M. S. Ghiorso and R. O. Sack (1995) Chemical mass transfer in magmatic processes; IV, A revised and internally-consistent thermodynamic model for the interpolation and extrapolation of liquid-solid equilibrium magmatic systems at elevated temperatures and pressures. *Contributions to*

Mineralogy and Petrology **119**(2-3), 197-212.

- [28] P. M. Smith and P. D. Asimow (2005) Adiatat\_1ph: A new public front-end to the MELTS, pMELTS, and pHMELTS models. *Geochemistry, Geophysics, Geosystems* **6**(2), Q02004, doi:10.1029/2004GC000816.
- [29] R. J. Stern et al. (2003) An Overview of the Izu-Bonin-Mariana Subduction Factory. *Geophysical Monograph* **138**, 175-222.
- [30] B. Taylor (1992) Rifting and the volcanic-tectonic evolution of the Izu Bonin-Mariana Arc. *Proc. Ocean Drill. Program Sci. Results* **126**, 627-651.
- [31] S. M. Straub (2003) The evolution of the Izu Bonin-Mariana volcanic arcs (NW Pacific) in terms of major element chemistry. *Geochemistry, Geophysics, Geosystems* **4**(2), 1018, doi: 10.1029/2002GC000357.
- [32] C. J. Bryant et al. (2003) The geochemical evolution of the Izu-Bonin arc system: A perspective from tephras recovered by deep-sea drilling. *Geochemistry, Geophysics, Geosystems* **4**(11), 1094, doi: 10.1029/2002GC000427.
- [33] A. G. Hochstaedter et al. (2000) Across-arc geochemical trends in the Izu Bonin arc: Constraints on source composition and mantle melting. *Journal of Geophysical Research* **105**, 495-512.
- [34] Y. Xu and S. W. Wise (1992) Middle Eocene to Miocene calcareous nanofossils of Leg 125 from the western Pacific Ocean. *Proc. Ocean Drill. Program Sci. Results* **125**, 43-70.
- [35] T. Plank and K. Kelley (2001) Contrasting Sediment Input and Output at the Izu and Mariana Subduction Factories. *EOS, Transactions, American Geophysical Union*, **82** (47), p. 1155.

- [36] S. M. Peacock et al. (2005) Thermal structure of the Costa Rica-Nicaragua subduction zone. *Physics of the Earth and Planetary Interiors* **149**(1-2), 187-200.
- [37] J. M. Eiler et al. (2005) Oxygen isotope constraints on the sources of Central American arc lavas. *Geochemistry, Geophysics, Geosystems* **6**(7), Q07007, doi: 10.1029/2004GC000804.
- [38] M. J. Carr (1984) Symmetrical and segmented variation of physical and geochemical characteristics of the Central American volcanic front. *Journal of Volcanological and Geothermal Research* **20**, 231-252.
- [39] M. J. Carr et al. (1990) Incompatible elements and isotopic evidence for the tectonic control of source mixing and melt extraction along the Central American arc. *Contributions to Mineralogy and Petrology* **105**, 369-380.
- [40] M. J. Carr et al. (2004) Volcanism and geochemistry in Central America: Progress and problems. *Geophysical Monograph* 138, 153-174.
- [41] G. A. Abers et al. (2003) The wet Nicaraguan slab. *Geophysical Research Letters* **30** (2), 1098, doi: 10.1029/2002GL015649.
- [42] W. P. Leeman et al. (1994) Boron geochemistry of the Central American volcanic arc: Constraints on the genesis of subduction-related magmas. *Geochimica et Cosmochimica Acta* **58**, 149-168.
- [43] L. C. Patino et al. (2000) Local and regional variations in Central American arc lavas controlled by variations in subducted sediment input. *Contributions to Mineralogy and Petrology* **138**, 265-283.
- [44] R. K. Workman and S. R. Hart (2005) Major and trace element composition of the depleted MORB mantle (DMM). *Earth and Planetary Science Letters* **231**(1-2), 53-

72, <http://dx.doi.org/10.1016/j.epsl.2004.12.005>.

- [45] B. R. Hacker et al. (2003) Subduction factory-1. Theoretical mineralogy, densities, seismic wave speeds, and H<sub>2</sub>O contents. *Journal of Geophysical Research-Solid Earth* **108**(B1), <http://dx.doi.org/10.1029/2001JB001129>.
- [46] C. R. Ranero et al. (2003) Bending-related faulting and mantle serpentinization at the Middle America trench. *Nature* **425**, 367-373.
- [47] J. M. Brenan et al. (1995) Mineral-aqueous fluid partitioning of trace elements at 900°C and 2.0 GPa: Constraints on the trace element chemistry of mantle and deep crustal fluids. *Geochimica et Cosmochimica Acta* **59**(16), 3331-3350.
- [48] E. Tenthorey and J. Hermann (2004) Composition of fluids during serpentinite breakdown in subduction zones: Evidence for limited boron mobility. *Geology* **32** (10), 865-868, doi: 10.1130/G20610.
- [49] M. T. McCulloch and A. J. Gamble (1991) Geochemical and geodynamical constraints on subduction zone magmatism. *Earth and Planetary Science Letters* **102**, 358-374.
- [50] M. Scambelluri et al. (2001) Fluid and Element Cycling in Subducted Serpentinite: A Trace-Element Study of the Erro-Tobbio High-Pressure Ultramafites (Western Alps, NW Italy). *Journal of Petrology* **42**(1), 55-67.
- [51] C. H. Langmuir et al. (2006) Chemical systematics and hydrous melting of the mantle in back-arc basins. *Geophysical Monograph* 166, 87-146.
- [52] T. V. Gerya and D. A. Yuen (2003) Rayleigh-Taylor instabilities from hydration and melting propel 'cold plumes' at subduction zones. *Earth and Planetary Science Letters* **212**, 47-62.
- [53] J. A. Pearce et al. (2005) Geochemical mapping of the Mariana arc-basin system:

implications for the nature and distribution of subduction components.

Geochemistry, Geophysics, Geosystems **6**(7), doi:10.1029/2004GC000895.

- [54] A. W. Hofmann (1988) Chemical differentiation of the Earth: the relationship between mantle, continental crust, and oceanic crust. *Earth and Planetary Science Letters* **90**, 297-314.
- [55] <http://www-rci.rutgers.edu/~carr/index.html>
- [56] E. A. Herrstrom et al. (1995) Variations in lava composition associated with flow of asthenosphere beneath southern Central America. *Geology* **23**(7), 617-620.
- [57] P. B. Kelemen et al. (2003) Thermal Structure due to Solid-State Flow in the Mantle Wedge. *Geophysical Monograph* 138, 293-311.
- [58] H. Keppler (1996) Constraints from partitioning experiments on the composition of subduction-zone fluids. *Nature* **380**, 237-240.
- [59] M. J. Carr et al. (2007) Element fluxes from the volcanic front of Nicaragua and Costa Rica. *Geochemistry, Geophysics, Geosystems* **8**(6), doi: 10.1029/2006GC001396.
- [60] J. C. Alt et al. (1986) An oxygen isotopic profile through the upper kilometer of the oceanic crust, DSDP hole 504B. *Earth and Planetary Science Letters* **80**, 217-229.
- [61] H. Staudigel et al. (1995) Large-scale isotopic Sr, Nd and O isotopic anatomy of altered oceanic crust-DSDP/ODP sites 417/418. *Earth and Planetary Science Letters* **130**, 169-185.
- [62] M. Magaritz and H. P. Taylor (1974) Oxygen and hydrogen isotope studies of serpentinization in Troodos Ophiolite complex, Cyprus. *Earth and Planetary Science Letters* **23**, 8-14.
- [63] J. D. Woodhead et al. (2001) Hafnium isotope evidence for 'conservative' element

- mobility during subduction zone processes. *Earth and Planetary Science Letters* **192**, 331-346.
- [64] J. D. Woodhead et al. (1993) High field strength and transition element systematics in island arc and back-arc basin basalts: evidence for multi-phase melt extraction and depleted mantle wedge. *Earth and Planetary Science Letters* **114**, 491-504.
- [65] J. H. Davies and A. Rowland (1997) Importance of temperature-dependent viscosity and hydraulic fracture on physical models of subduction zone magmatism. *Geological Society of Australia Abstracts* **45**, 17-20.
- [66] J. Nakajima et al. (2005) Quantitative analysis of the inclined low-velocity zone in the mantle wedge of northeastern Japan: A systematic change of melt-filled pore shapes with depth and its implications for melt migration. *Earth and Planetary Science Letters* **234**, 59-70.
- [67] E. M. Stolper and S. Newman (1994) The role of water in the petrogenesis of Mariana Trough magmas. *Earth and Planetary Science Letters* **121**, 293-325.
- [68] B. Taylor and F. Martinez (2003) Back-arc basin basalt systematics. *Earth and Planetary Science Letters* **210**, 481-497.
- [69] K. A. Kelley et al. (2006) Mantle melting as a function of water content beneath back-arc basins. *Journal of Geophysical Research* **111**(B9), B09301.
- [70] L. H. Rupke et al. (2004) Serpentine and the subduction zone water cycle. *Earth and Planetary Science Letters* **223**, 17-34.
- [71] D. W. Peate and J. A. Pearce (1998) Causes of spatial compositional variations in Mariana arc lavas: Trace element evidence. *The Island Arc* **7**, 479-495.
- [72] <http://georoc.mpch-mainz.gwdg.de/georoc/>

## Figure Captions

**Figure 1:** (a) Schematic view of the GyPSM-S model calculation space. Sample columns are shown, as well as locations of fluid release and melt initiation. The layered structure of the subducting crust is detailed in addition to initial water content. (b) Schematic view of a single calculation column showing a phase boundary within the slab and the effective water release point ( $P_s, T_s$ ) as a dark blue filled circle. The successive equilibration points above the inclined slab-wedge interface are filled black circles labeled  $(P_0, T_0) \dots (P_n, T_n)$ , where the final point (red) represents melt initiation where the activity of water drops below unity for the equilibrium assemblage.

**Figure 2:** Simplified phase diagrams for MORB (a) and harzburgite (b) from [45] with example pressure-temperature trajectories for slab particles from the NIB model case (yellow) and the CCR model case (red). The trajectories for the different models cross different phase boundaries due to the different thermal structures experienced by the slab, respectively. For the MORB case, I: prehnite-pumpellyite facies, containing 4.5 wt. %  $H_2O$ ; II: lawsonite blueschist, containing 5.0 wt. %  $H_2O$ ; III: lawsonite amphibole eclogite, containing 3.0 wt. %  $H_2O$ ; IV: amphibole eclogite, containing 1.0 wt. %  $H_2O$ ; V: amphibolite, containing 1.3 wt. %  $H_2O$ ; VI: epidote amphibolite, containing 2.0 wt. %  $H_2O$ ; VII: greenschist facies, containing 3.0 wt. %  $H_2O$ . For the harzburgite case, I: rock containing serpentine chlorite brucite, with 14.8 wt. %  $H_2O$ ; II: assemblage containing high-pressure hydrous phase A, containing 6.8 wt. %  $H_2O$ ; III: serpentine chlorite dunite,

containing 6.2 wt. % H<sub>2</sub>O; IV: chlorite harzburgite, containing 1.4 wt. % H<sub>2</sub>O; V: garnet harzburgite, containing 0.0 wt. % H<sub>2</sub>O.

**Figure 3:** Results from GyPSM-S calculations showing the thermal structure and example particle fluid release points for models (a) ADD1, (b) NIB, (c) ADD2, (d) CCR, (e) SCR, and (f) NMAR (Table 3). Fluid mass releases (in ppm) are noted for all models (see Fig. 2 for dehydration reaction information), and the calculation columns for this study are noted for the NIB and CCR models. Pressures (in bars) are noted on the left-hand side of the figures and arrows indicate lateral extents of fluid infiltration in (e, f).

**Figure 4:** Initial concentrations of fluid-mobile elements used in this study (Ba, Th, U, Pb, and Sr) for immediate fluid releases calculated in equilibrium with serpentinized lithosphere (gray) or AOC (black) source lithologies. Different lines indicate different initial fluid masses released from different reactions within the slab (see Fig. 2 and 3).

**Figure 5:** Plot of total degree of melting (F) experienced by the advecting mantle material at different distances from the slab for CCR (black) and NIB (gray). The maximum melt fractions are extracted from ~15-25 km vertical distance from the slab, initiated from mid-pressure fluid-releases.

**Figure 6:** Plots of the changing activity of water in the system for (a) the NIB model and (b) the CCR model. The thickness of the hydrated channel adjacent to the slab (LVC) is water-saturated ( $a_{H_2O} = 1.0$ ). When melting initiates, water partitions into the melt phase,

and the activity of water rapidly decreases after that point. The initial activities are all equal to 1.0, but are spread out slightly in the y-direction on the plot for clarity.

**Figure 7:** Cartoon of the LVC, slab fluid releases, and melting regions for an example mature-slab model with a moderate slab dip angle. Indicated are potential simple melt migration pathways that would allow deeper melts to impact rear-arc lava chemistry and shallower melts to impact volcanic front (VF) lava chemistry. The trends observed by [15, 19] for cross-arc variations reflecting distance to WBZ are shown.

**Figure 8:** Plots of modeled trace element ratios for the limited fluid interaction case: (a, b) indicators of progressive mantle source depletion as a function of slab fluid source lithology and dehydration pressure (MORB value for  $Zr/Nb \sim 30$  [15] and for  $Nb/Yb \sim 0.92$  [54]); (c-e) indicators of degree of hydration ( $U/Th$ ) versus dehydration pressure and degree of mantle source depletion as a function of slab fluid source lithology and compared to regional datasets [55, 72]; (f, g) indicators of mantle source enrichment ( $La/Yb$ ) versus indicators of slab fluid contribution ( $Ba/La$ ) as a function of slab fluid source lithology and compared to regional datasets.

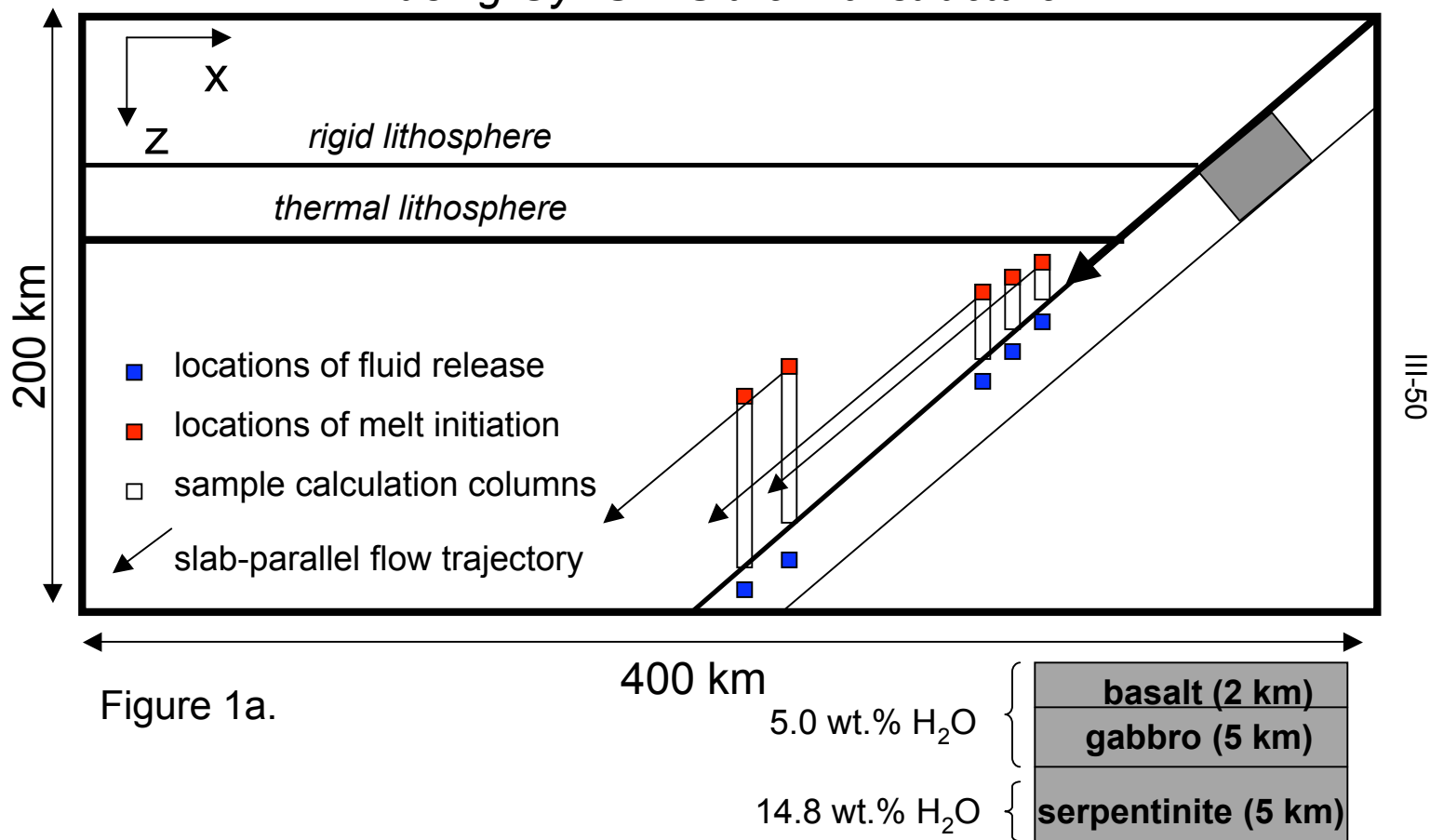
**Figure 9:** Plots of modeled trace element ratios for the limited fluid interaction case: (a, b) ratios of fluid-mobile elements to HFSE as a function of slab fluid source lithology and dehydration pressure and (c-f) versus indicators of slab fluid contribution and compared to regional datasets [55, 72].

**Figure 10:** Schematic diagrams for the extension of the calculation column for the fully-equilibrated case at lower pressures (a, b) and at higher pressures (c, d). The columns for the two cases are not extended the same vertical distance.

**Figure 11:** Fractionation paths for a calculated primary Miyakejima magma composition, plotted with the Miyakejima lava dataset [72].

**Figure 12:** Schematic models for transport of fluids and/or melts to the back-arc melting region: (a) in this model, which is similar to the ultimate development of the mature slab system (Chapter 2), continuous fluxing of the deep melt region by a strong serpentinite-derived fluid source results in progressive lengthening of the fluid pathway such that low-pressure, hydrous melts can be generated by direct delivery of fluids to the base of the BABB melting region. (b) Diapiric rise of hydrous melts generated at depth transport material to the base of the BABB melting region. (c) Melt transport along a vertical path beyond the water-saturated solidus results in a freezing of the melt into an enriched mantle packet, which is transported along solid streamlines to the base of the BABB melting region.

using GyPSM-S thermal structure



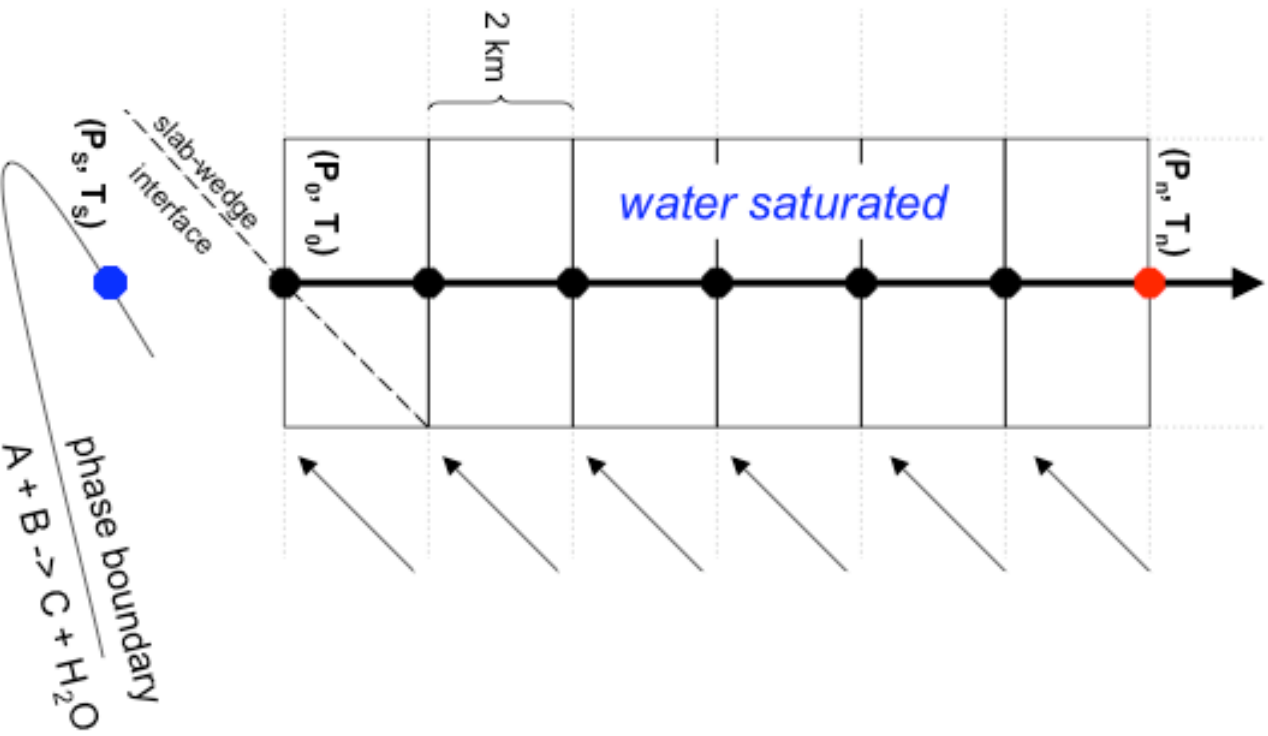
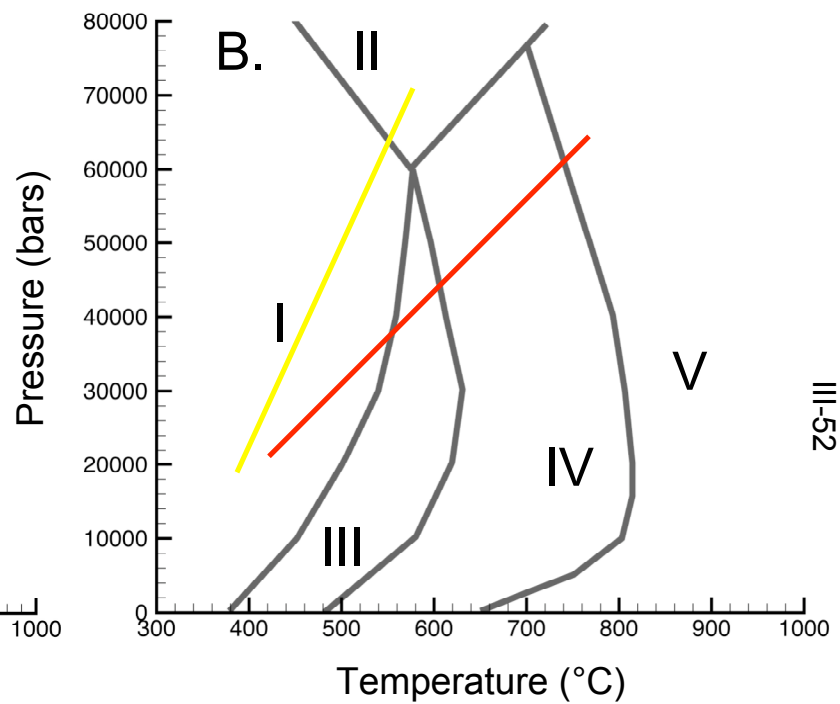
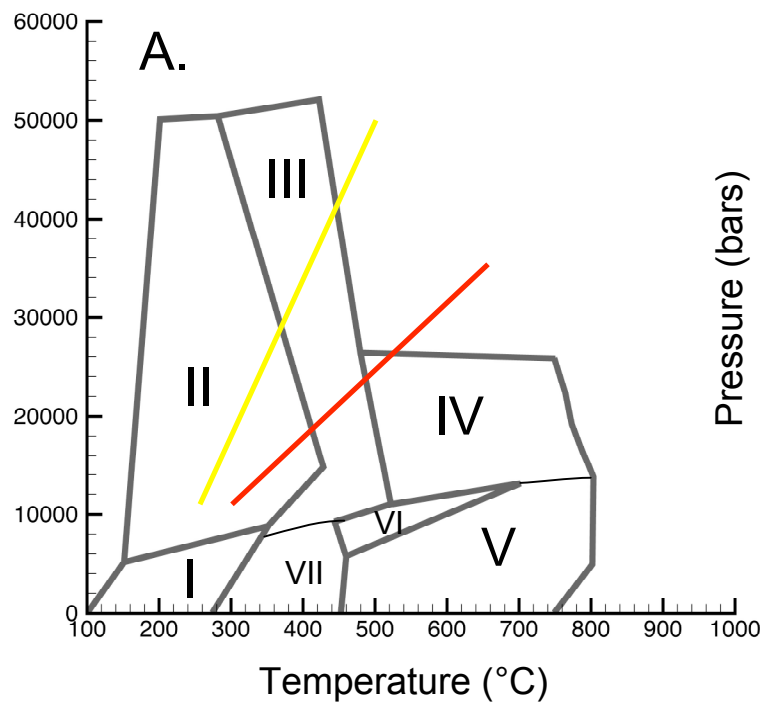


Figure 1b.



III-52

Figure 2.

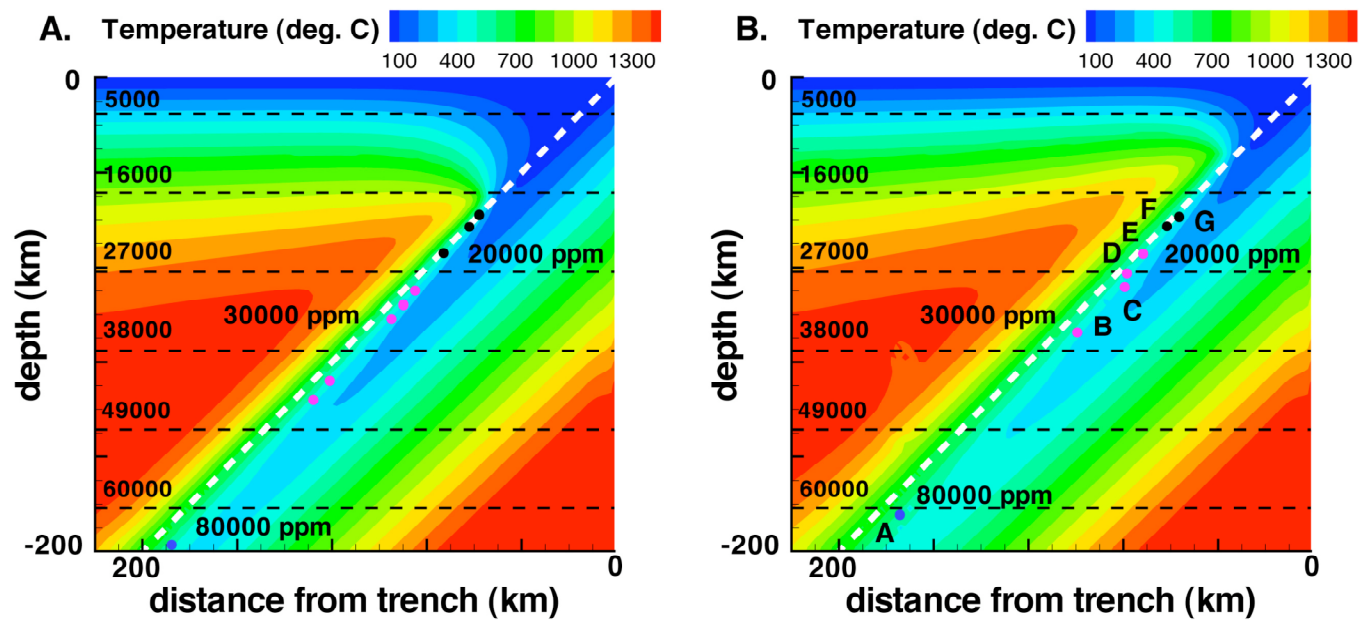
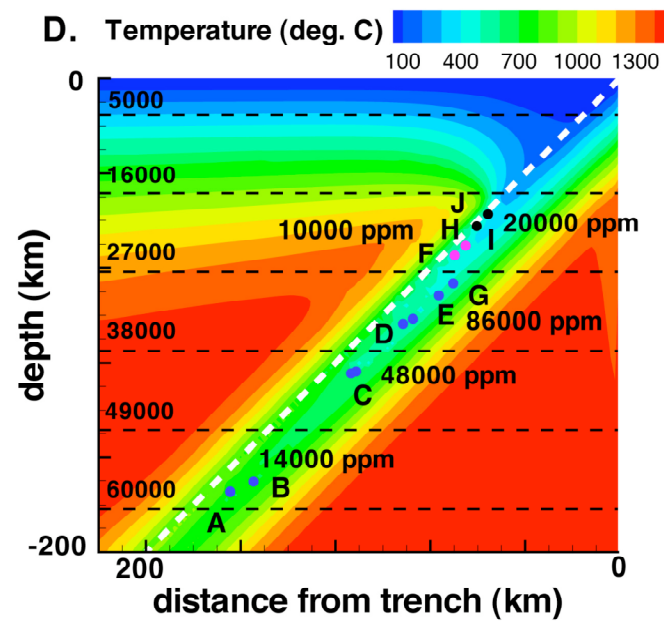
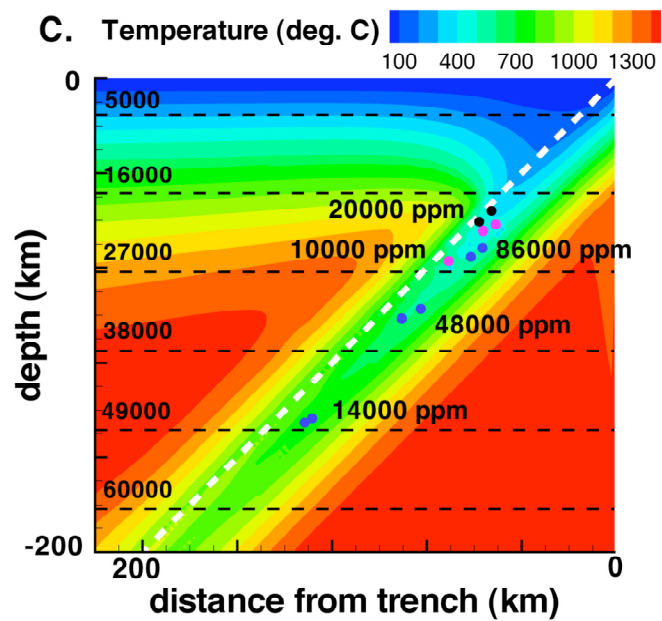
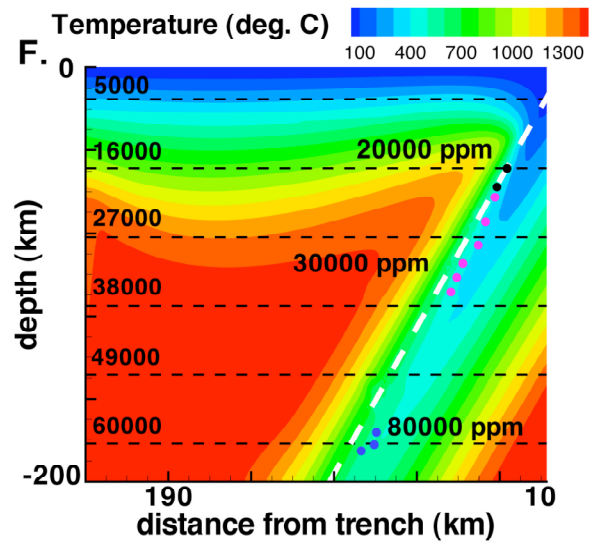
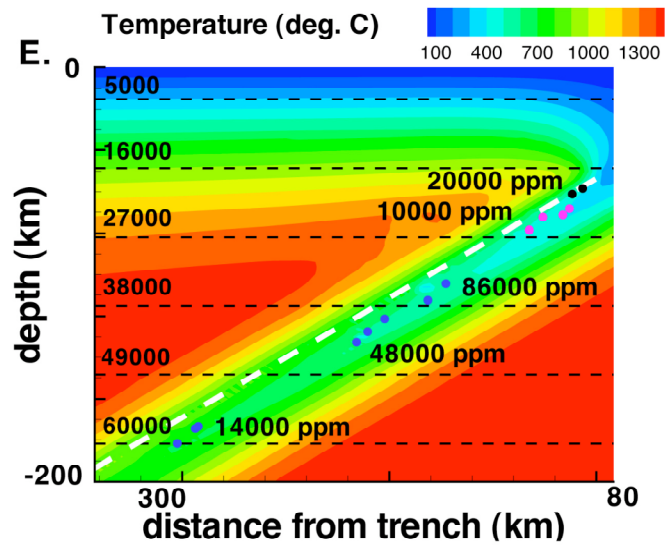


Figure 3.





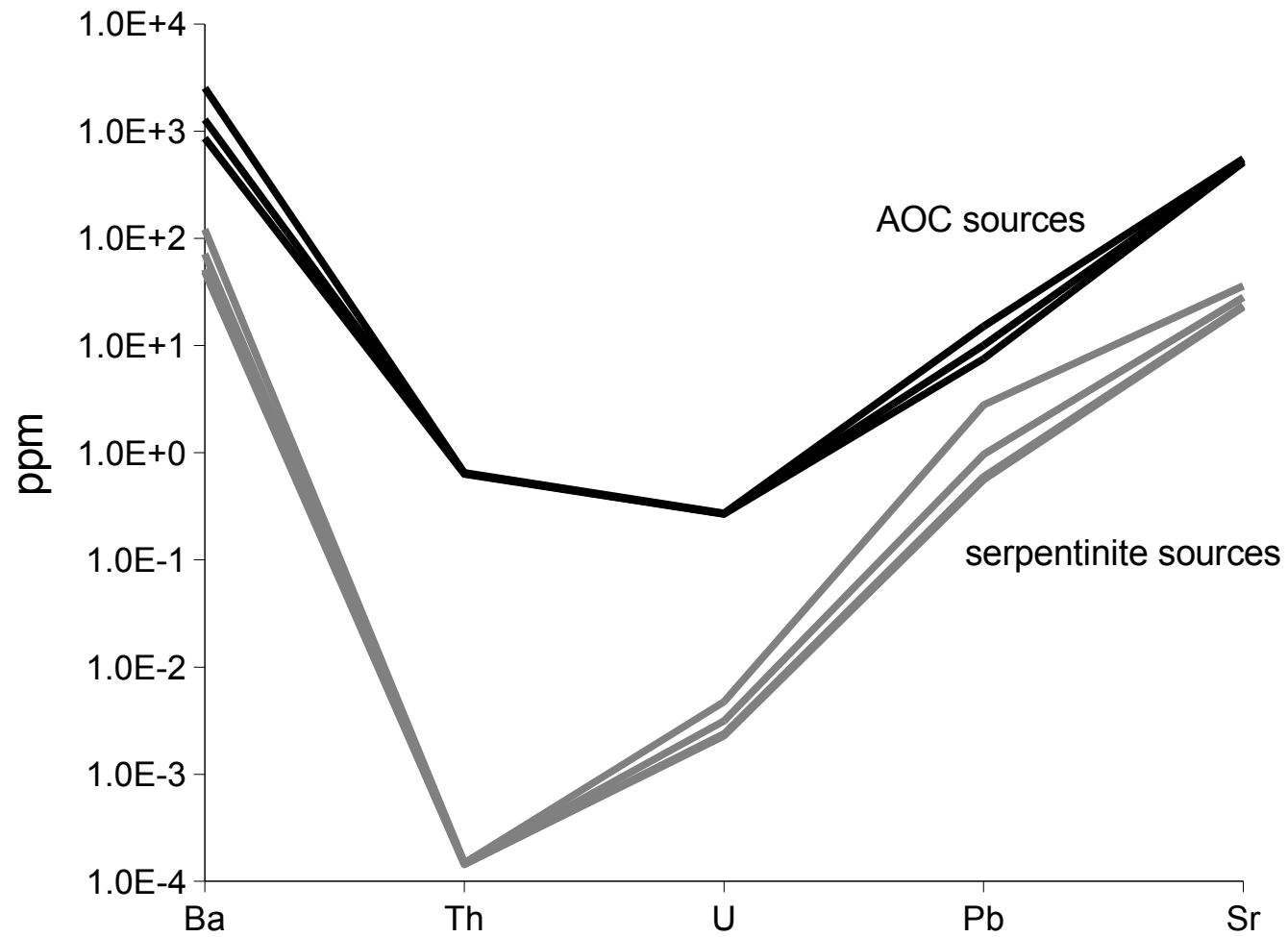
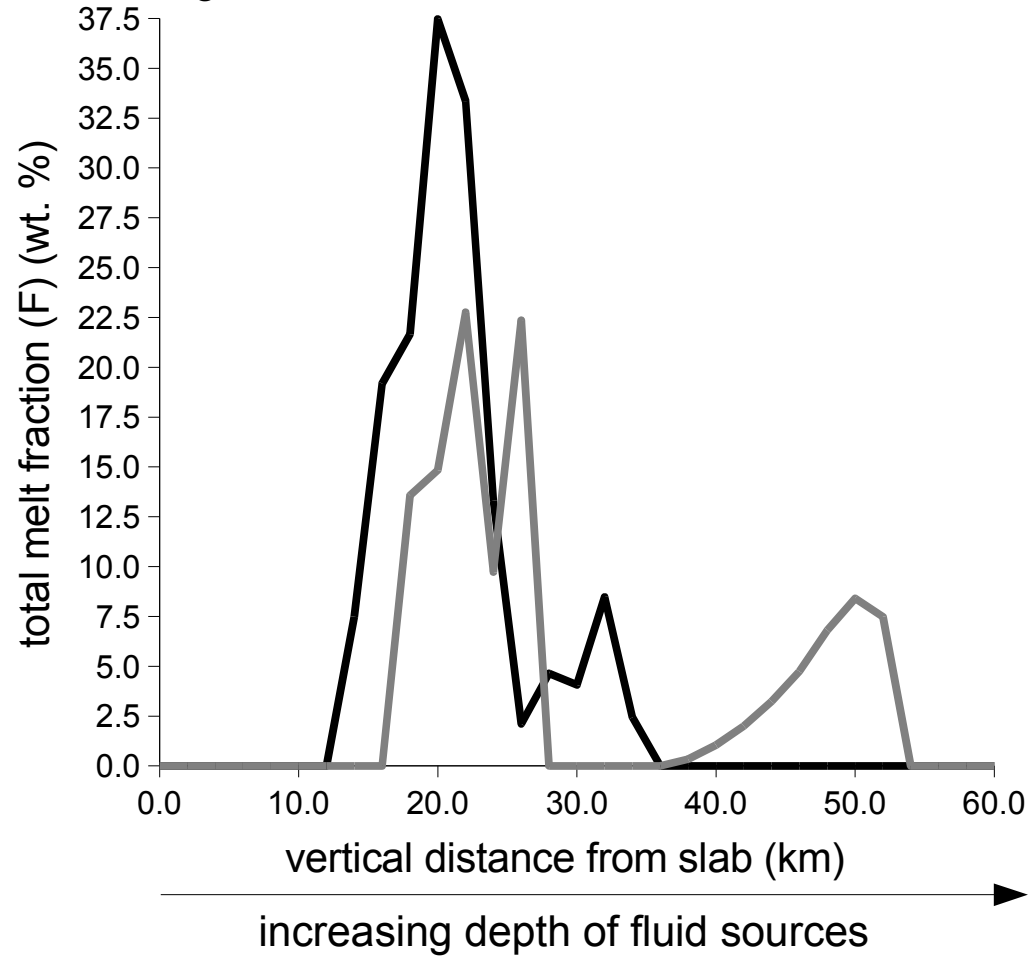


Figure 4.

Figure 5.



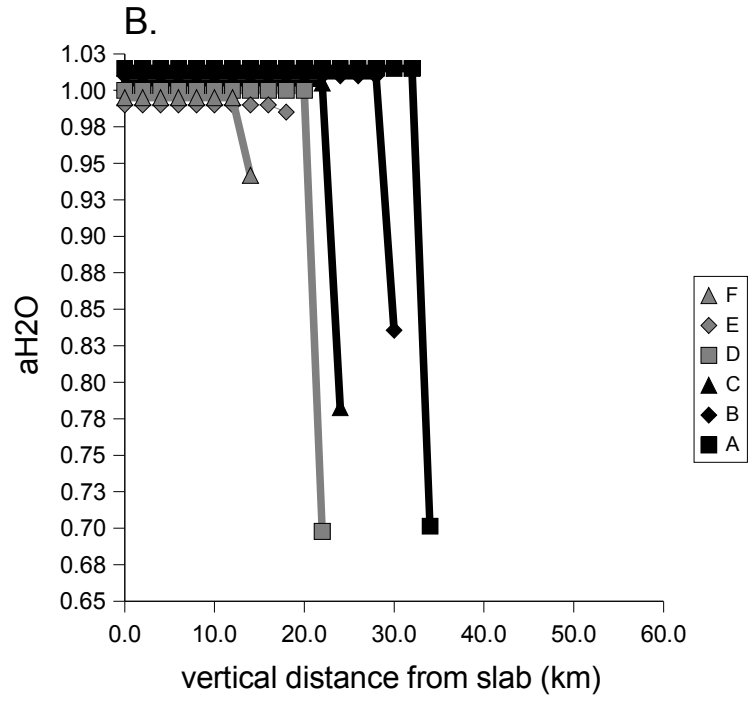
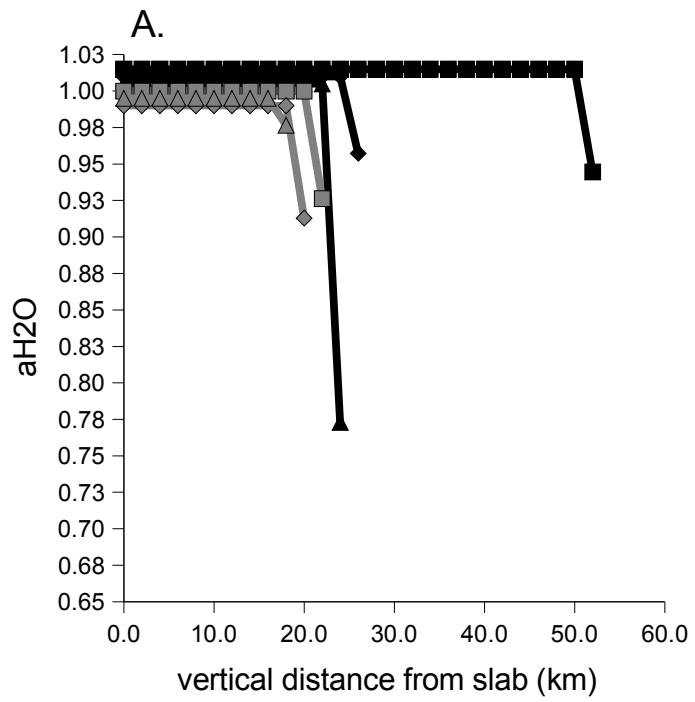


Figure 6.

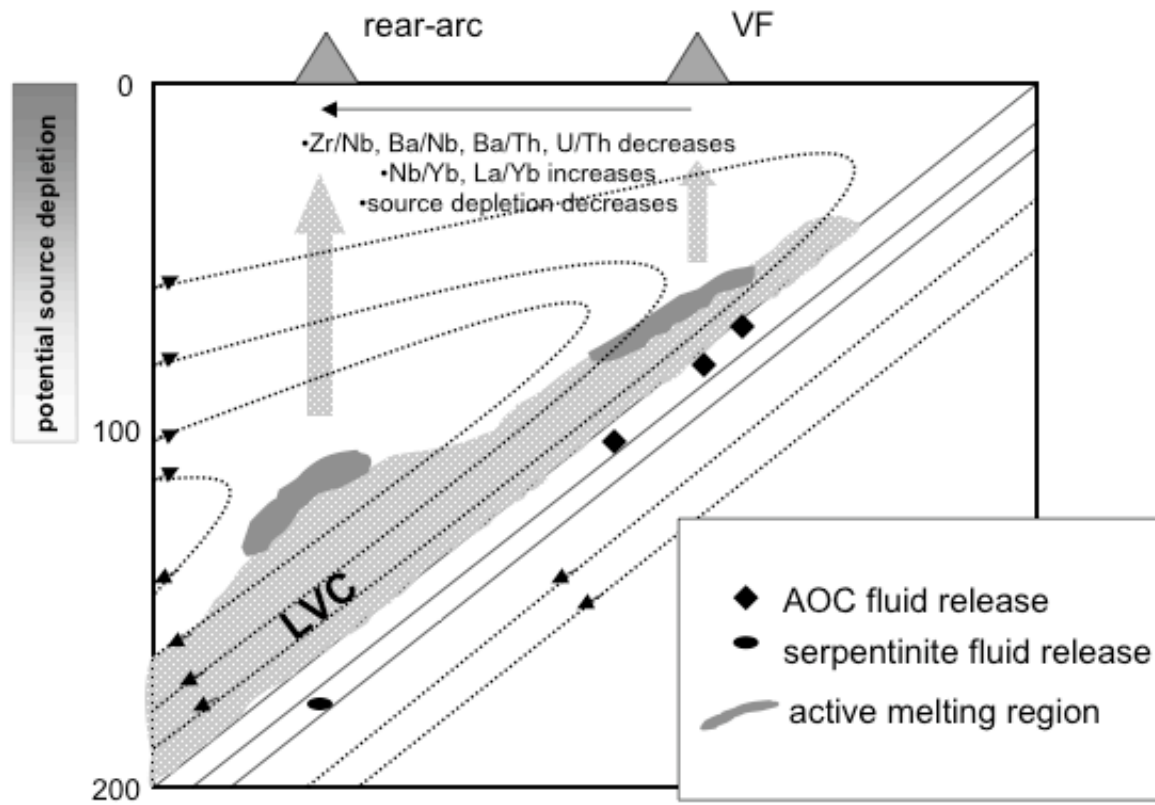
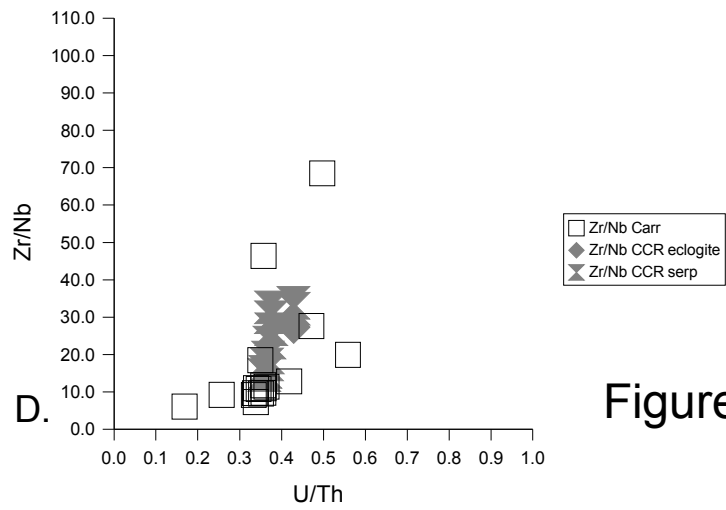
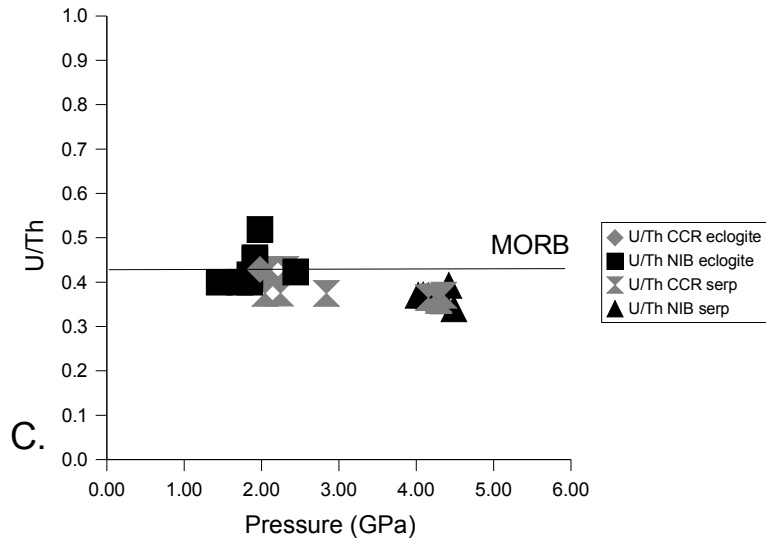
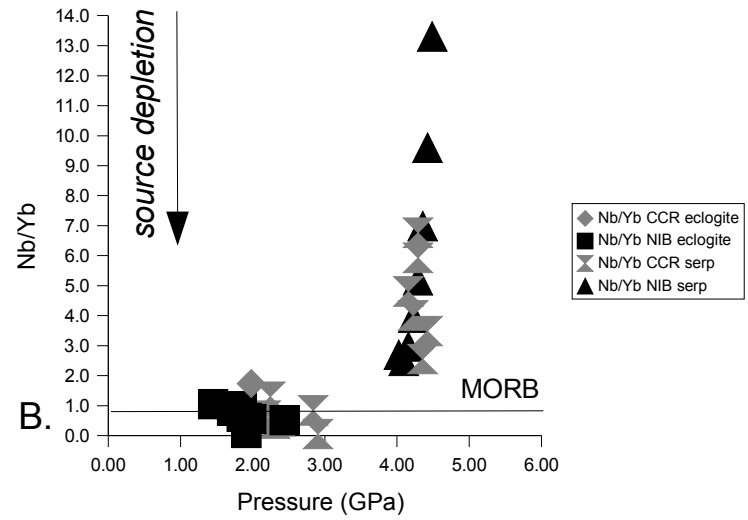
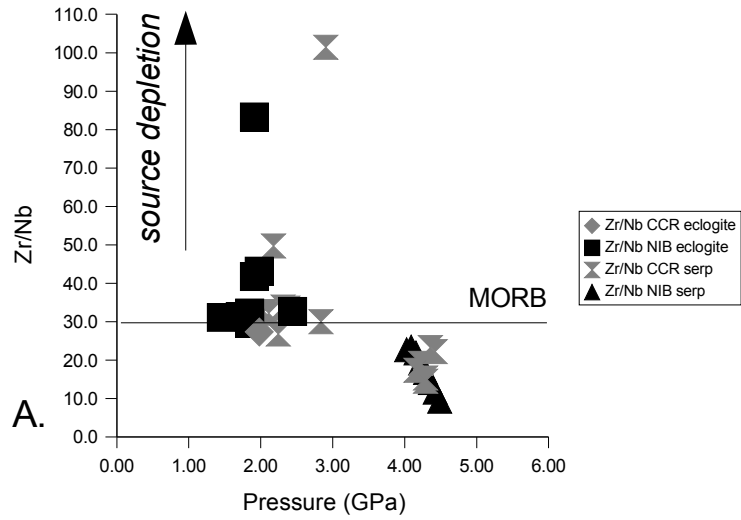
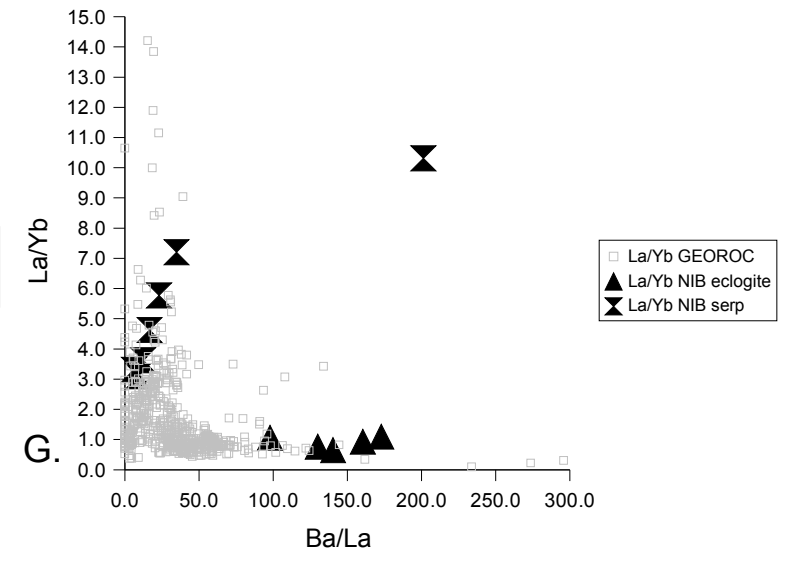
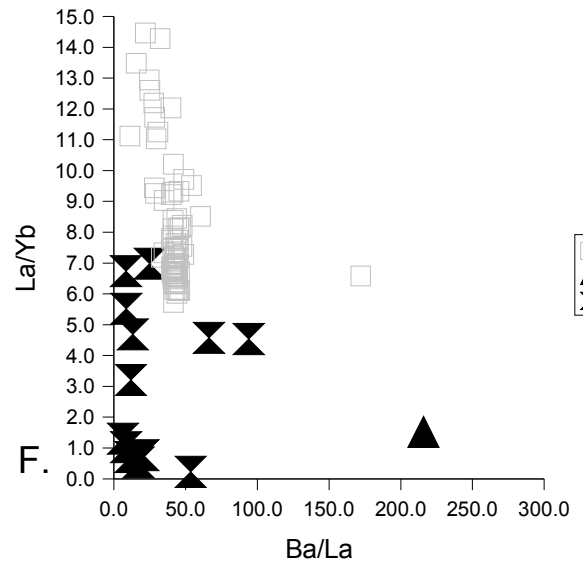
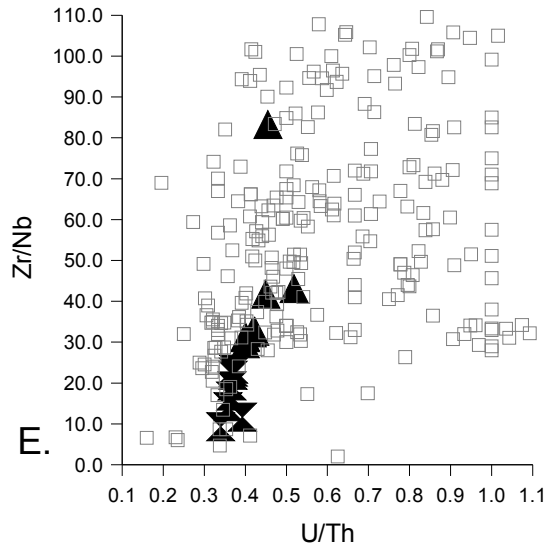


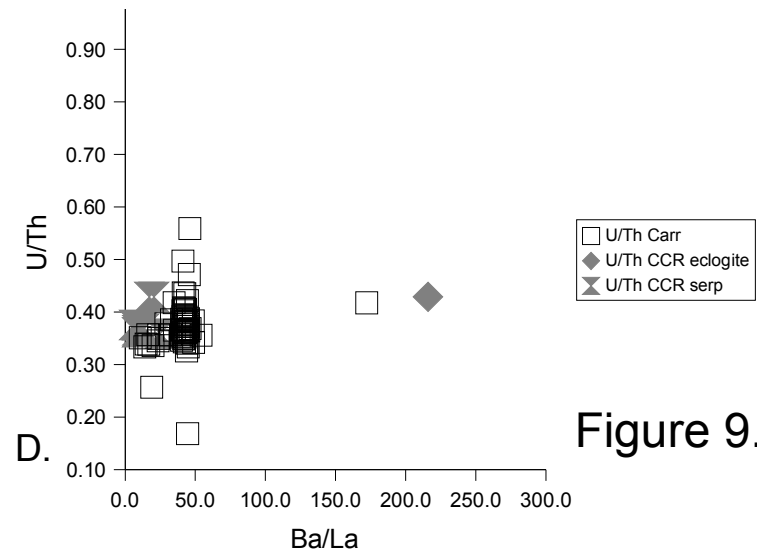
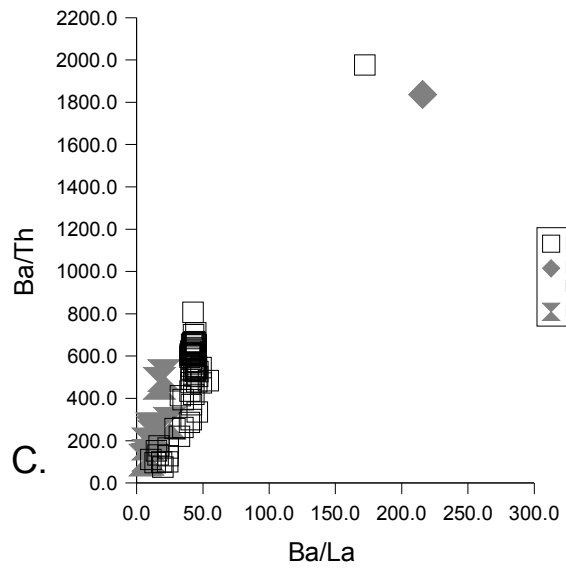
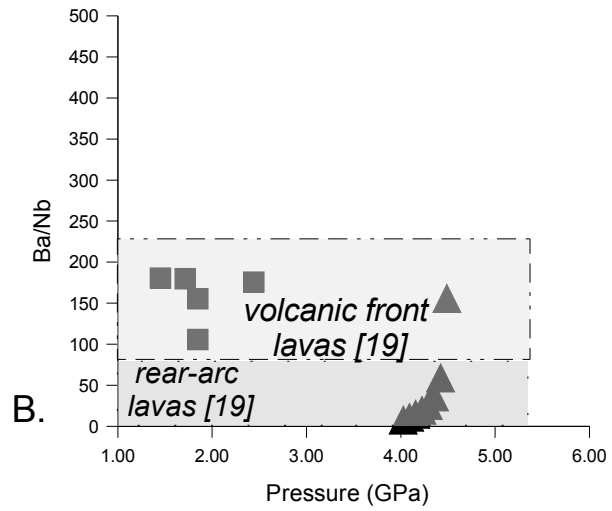
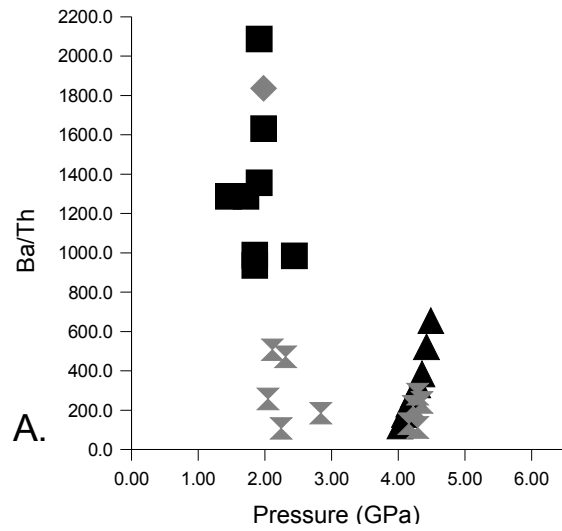
Figure 7.



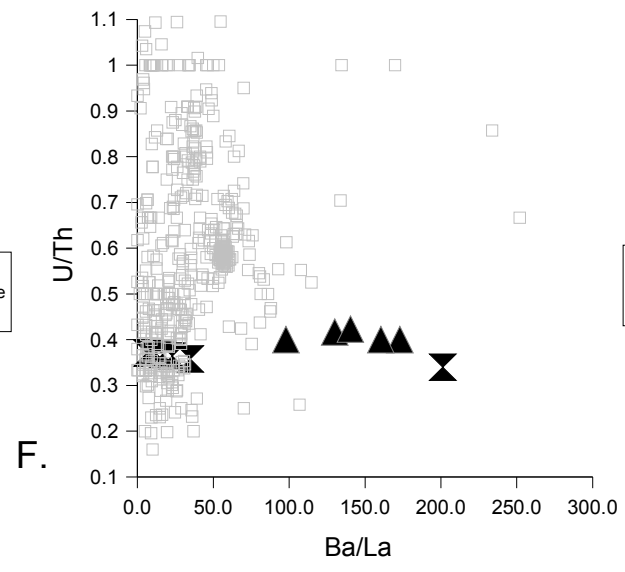
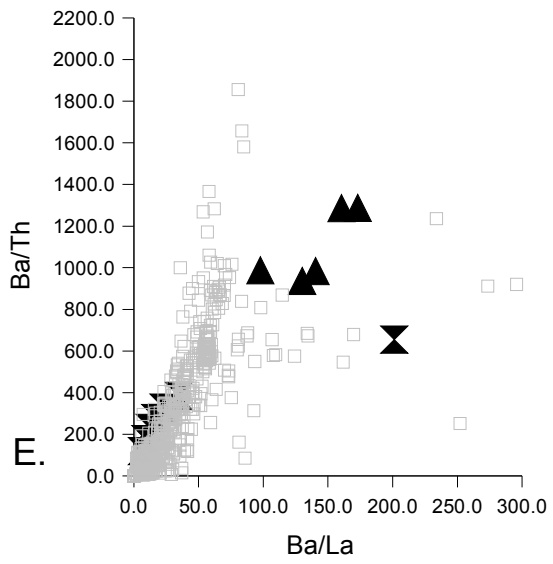
09-III

Figure 8.





**Figure 9.**



III-63

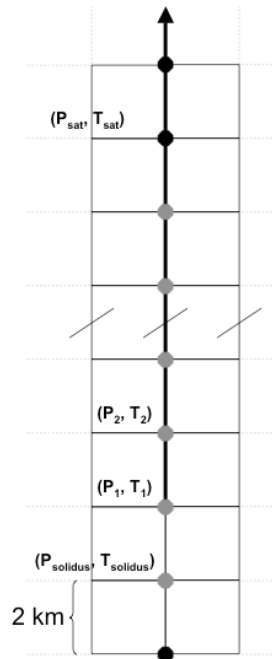
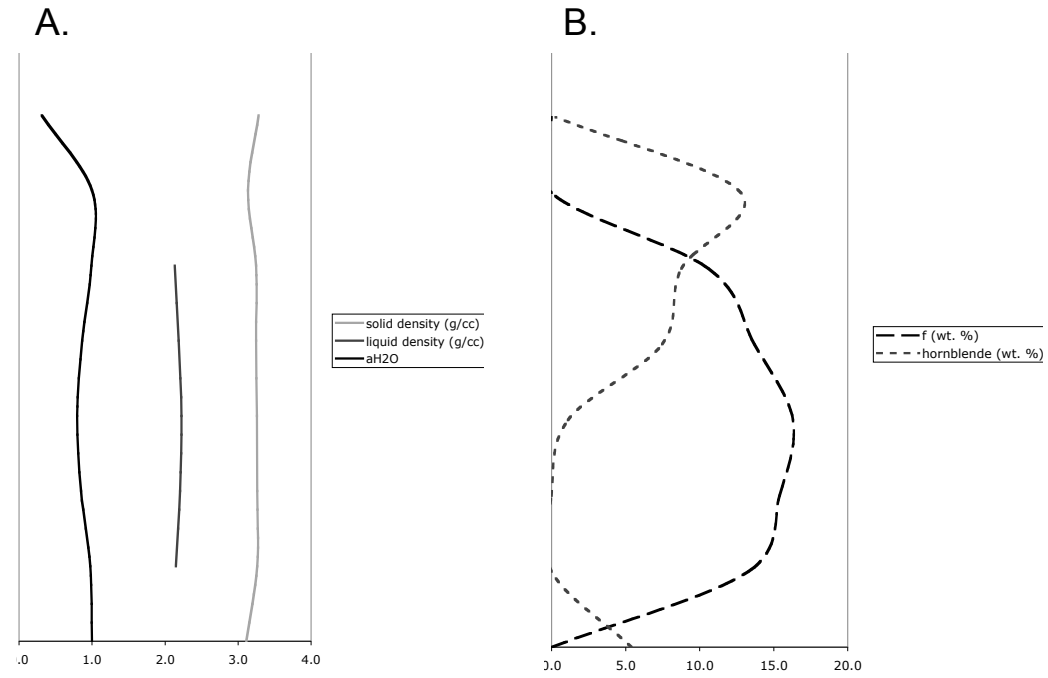
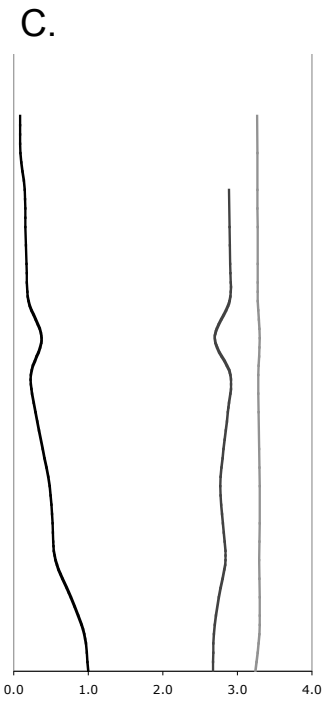
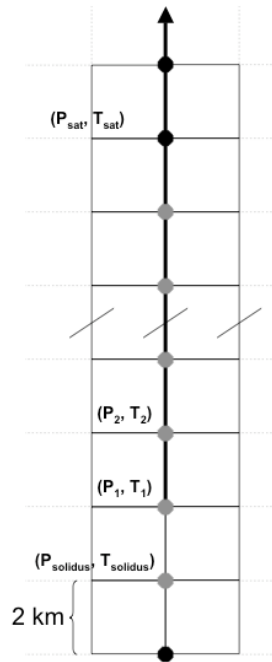


Figure 10.





III-65

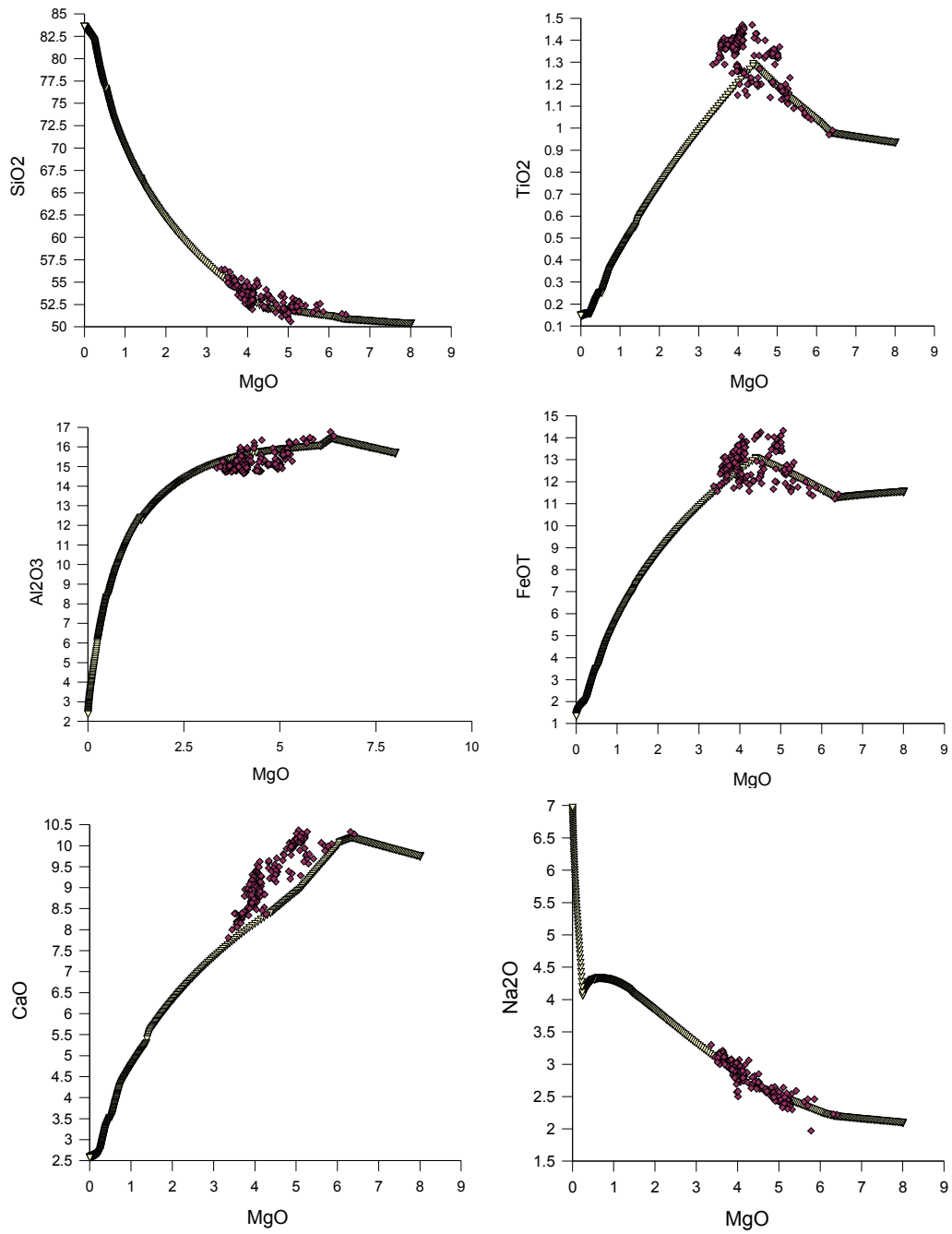


Figure 11.

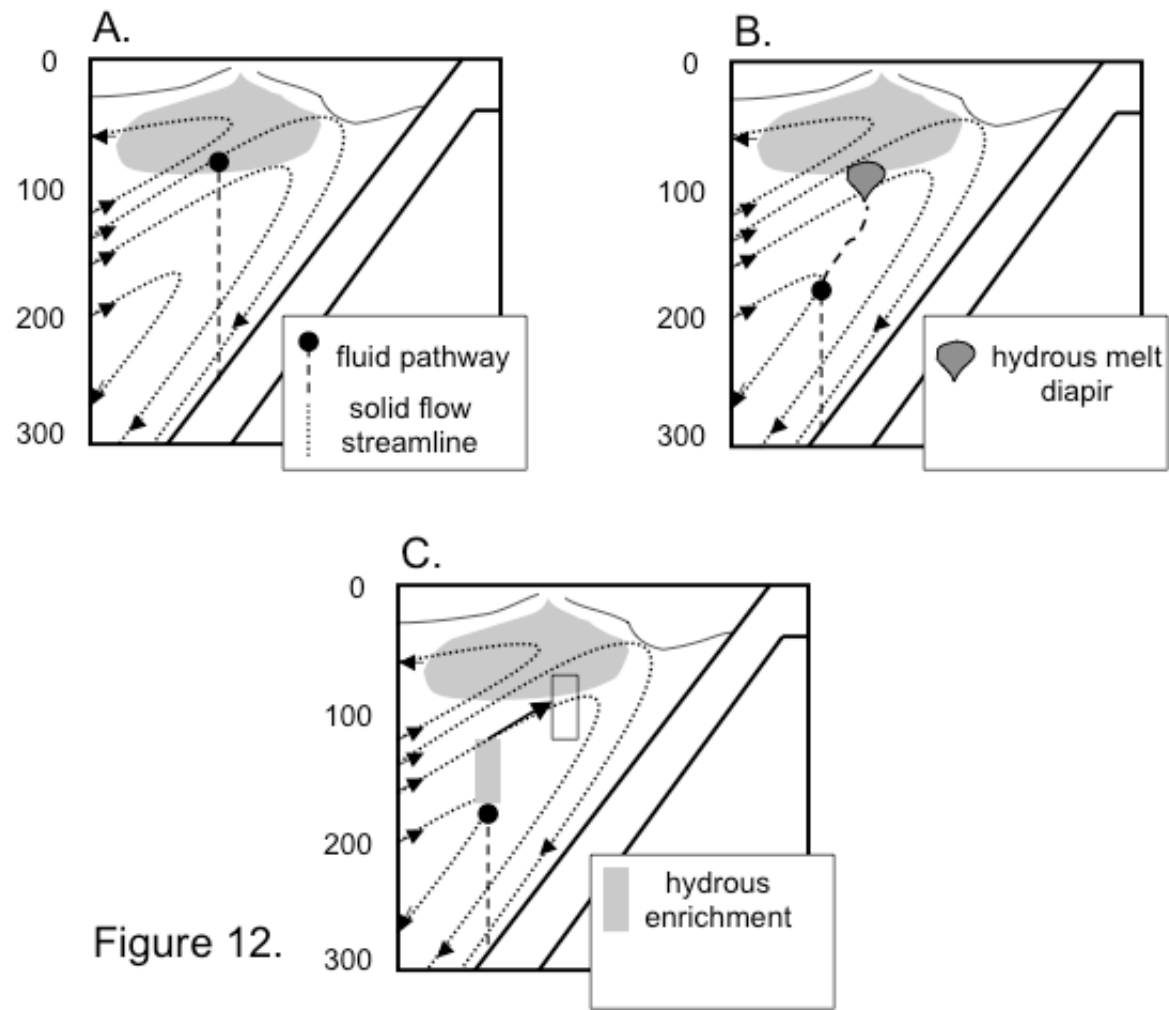


Figure 12.

Table 1: pHMELTS starting composition

<b>oxide</b>	<b>initial value (weight percent)</b>
SiO <sub>2</sub>	44.80
TiO <sub>2</sub>	0.13
Al <sub>2</sub> O <sub>3</sub>	3.99
Fe <sub>2</sub> O <sub>3</sub>	0.41
Cr <sub>2</sub> O <sub>3</sub>	0.57
FeO	7.83
MgO	38.81
CaO	3.18
Na <sub>2</sub> O	0.28
<b>tracer</b>	<b>initial value (ppm)</b>
H <sub>2</sub> O	110.00
K	60.00
Rb	0.05
Ba	0.56
Th	0.01
U	0.0032
Nb	0.15
Ta	0.01
La	0.19
Ce	0.55
Pb	0.02
Pr	0.11
Nd	0.58
Sr	7.66
Zr	5.08
Hf	0.16
Sm	0.24
Eu	0.10
Ti	716.30
Gd	0.36
Tb	0.07
Dy	0.51
Ho	0.12
Y	3.33
Er	0.35
Yb	0.37
Lu	0.06

*Adapted from Workman and Hart [44]*

Table 2: Partition coefficients and sample column calculation

<i>trace elements (fluid-mobile)</i>	initial ppm serpentinite	initial ppm AOC	$D_{\text{serpentinite/fluid}}$	$D_{\text{eclogite/fluid}}$	$D_{\text{lherzolite/fluid}}$
<b>Ba</b>	5.7000	26.0000	0.0333	0.0002	7.60E-005
<b>Th</b>	0.0001	0.2700	0.6667	0.4100	0.0890
<b>U</b>	0.0003	0.1400	0.0500	0.5100	0.0250
<b>Pb</b>	0.0500	0.3000	0.0040	0.0100	3.10E-003
<b>Sr</b>	4.0500	110.0000	0.1000	0.1900	0.0430
<b>reference</b>	(a)	(b)	(c)	(d)	(e)

Notes: Fluids are assumed to be released in trace element equilibrium from the source lithology (assuming to start with 100.0 g). For example, 0.5 wt. % (0.5 g) fluid fraction released from the AOC layer, using Equation (1) and the values for  $D^{\text{eclogite/fluid}}$  given above, will result in a fluid carrying approximately 4972.41 ppm Ba, 0.65 ppm Th, 0.27 ppm U, 20.07 ppm Pb, and 566.86 ppm Sr.

If this fluid (0.5 g) is then added to 100.0 g of water-saturated subsolidus lherzolite at ( $P_0, T_0$ ) (Table 1, assuming the composition has not been subject to prior melt depletion), the resulting bulk fluid-mobile trace element composition of the lherzolite + fluid assemblage (100.5 g) will include 25.3 ppm Ba, 0.01 ppm Th, 0.005 ppm U, 0.118 ppm Pb, and 10.46 ppm Sr.

This fluid, after equilibrating with the lherzolite, is then moved along to the next equilibration point ( $P_1, T_1$ ). Using Equation (1) and the values for  $D^{\text{lherzolite/fluid}}$  given above, the bulk composition of the 0.5 g of fluid equilibrated at ( $P_0, T_0$ ) and removed to ( $P_1, T_1$ ) is 4984.61 ppm Ba, 0.107 ppm Th, 0.167 ppm U, 14.60 ppm Pb, and 218.90 ppm Sr.

If this fluid (0.5 g) is then added to 100.0 g of lherzolite at ( $P_1, T_1$ ), the resulting bulk fluid-mobile trace element composition of the lherzolite + fluid assemblage (100.5 g) will include 25.36 ppm Ba, 0.008 ppm Th, 0.004 ppm U, 0.091 ppm Pb, and 8.72 ppm Sr.

This is repeated to ( $P_{\text{solidus}}, T_{\text{solidus}}$ ) when the water-saturated solidus is crossed, and melting initiates. At that point, pHMELTS calculates the melt and residue trace element composition based on the lherzolite+fluid bulk composition.

- 
- (a) serpentinite ETF1 from Scambelluri et al. [50] Supp. Mat.
  - (b) altered oceanic crust composition from McCulloch and Gamble [49]
  - (c) Tenthorey and Hermann [48] best estimates of partition coefficients, U and Sr are lower estimates
  - (d) Brenan et al. [47] calculated eclogite/fluid partition coefficients
  - (e) Brenan et al. [47] calculated lherzolite/fluid partition coefficients
-

Table 3: A summary of subduction zone model parameters

<b>approximate subduction region</b>	Central Costa Rica	Southeastern Costa Rica	Northern Izu-Bonin	Northern Mariana	Additional Model 1	Additional Model 2
<b>abbreviation</b>	CCR	SCR	NIB	NMAR	ADD1	ADD2
<b>latitude</b>	~8-11° N	~8-11° N	~32° N	~23° N	N/A	N/A
<b>longitude</b>	~275-277° E	~276-278° E	~135-143° E	~143-145° E	N/A	N/A
<b>rate of convergence (mm/yr)</b>	87 [36]	90 [36]	50 [29]	47.5 [29]	87.00	50.00
<b>slab dip (degrees)</b>	45 [36]	30 [36]	45 [29]	60 [29]	45	45
<b>slab thermal age (Ma)</b>	18 [36]	15 [36]	135 [29]	165 [29]	135	18
<b>rigid lithospheric thickness (km)</b>	50 [36]	50 [36]	32 [71]	32 [71]	50	50
<b>thermal lithospheric thickness (km)</b>	88	88	66	66	88	88
<b>dimensional grid resolution (z, x)</b>	2.0 km, 2.0 km	2.0 km, 3.4641 km	2.0 km, 2.0 km	2.0 km, 1.1547 km	2.0 km, 2.0 km	2.0 km, 2.0 km
<b>dimensions of model domain (z, x)</b>	200 km, 400 km	200 km, 692.8 km	200 km, 400 km	200 km, 230.9 km	200 km, 400 km	200 km, 400 km

*numbers in square brackets are references*

Table 4: Major element chemistry of modeled initial melts

Major Oxides (wt. %)	CCR_F14L	CCR_E14L	CCR_E16L	CCR_E18L	CCR_D18L	CCR_D20L	CCR_D22L	CCR_C22L	CCR_C24L	CCR_B26L	CCR_B28L	CCR_B30L	CCR_A30L	CCR_A32L	CCR_A34L
SiO <sub>2</sub>	42.45	40.61	42.51	43.49	41.01	43.57	41.84	39.65	38.99	36.54	36.68	37.15	36.56	37.00	37.45
TiO <sub>2</sub>	0.24	0.26	0.32	0.34	0.41	0.32	0.35	0.33	0.41	0.91	0.83	0.88	0.89	0.73	0.96
Al <sub>2</sub> O <sub>3</sub>	18.00	17.11	14.69	14.17	12.52	10.08	15.62	9.11	11.58	2.49	2.72	3.02	2.05	2.31	2.58
Fe <sub>2</sub> O <sub>3</sub>	0.55	0.67	0.80	0.82	1.03	0.86	0.70	0.87	0.97	1.65	1.77	1.78	1.98	1.70	1.83
Cr <sub>2</sub> O <sub>3</sub>	0.41	0.41	0.60	0.61	0.58	0.80	0.26	0.61	0.33	0.79	0.62	0.56	0.55	0.52	0.52
FeO	5.42	6.37	6.08	5.87	7.63	6.62	7.93	9.00	10.39	15.51	15.63	15.85	16.60	15.72	16.55
MgO	8.62	9.87	10.63	10.54	13.04	14.00	12.42	18.63	17.50	21.92	23.40	23.43	24.32	25.40	24.05
CaO	6.18	6.68	7.65	7.86	8.33	8.12	7.65	8.98	8.57	4.42	5.37	5.22	5.16	5.95	4.79
Na <sub>2</sub> O	3.03	2.21	1.28	1.15	0.86	0.69	3.24	0.25	1.74	5.79	3.75	4.38	3.47	2.45	5.01
H <sub>2</sub> O	15.10	15.81	15.44	15.15	14.59	14.94	9.98	12.56	9.53	9.98	9.23	7.73	8.43	8.21	6.26
Temperature (deg. C)	1116.59	1137.11	1153.33	1153.95	1201.91	1213.20	1234.69	1295.70	1312.51	1359.62	1379.62	1396.22	1395.51	1408.88	1419.34
Pressure (bars)	19800.00	21780.00	21120.00	20460.00	23760.00	23100.00	22440.00	29040.00	28380.00	42900.00	42240.00	41580.00	44220.00	43560.00	42900.00

(a)

Major Oxides (wt. %)	NIB_F18L	NIB_E20L	NIB_D20L	NIB_D22L	NIB_C20L	NIB_C22L	NIB_C24L	NIB_B26L	NIB_A38L	NIB_A40L	NIB_A42L	NIB_A44L	NIB_A46L	NIB_A48L	NIB_A50L	NIB_A52L
SiO <sub>2</sub>	47.83	45.83	43.54	45.15	42.97	45.11	44.86	40.89	36.55	36.53	36.53	36.58	36.68	36.85	36.98	37.10
TiO <sub>2</sub>	0.22	0.28	0.29	0.32	0.30	0.38	0.30	0.34	0.94	0.95	0.93	0.89	0.83	0.76	0.70	0.72
Al <sub>2</sub> O <sub>3</sub>	18.19	16.83	16.36	15.26	16.11	13.17	16.83	12.79	1.91	2.08	2.27	2.48	2.72	2.99	3.28	3.57
Fe <sub>2</sub> O <sub>3</sub>	0.59	0.69	0.73	0.78	0.74	0.91	0.67	0.85	1.20	1.46	1.66	1.76	1.77	1.70	1.62	1.65
Cr <sub>2</sub> O <sub>3</sub>	0.49	0.45	0.55	0.52	0.57	0.62	0.31	0.55	1.24	0.97	0.79	0.68	0.61	0.57	0.56	0.54
FeO	3.48	4.74	5.28	5.30	5.52	5.63	5.80	7.58	14.79	15.39	15.72	15.78	15.63	15.29	14.91	14.94
MgO	6.25	8.27	8.91	9.44	9.21	10.17	9.70	13.71	19.76	21.05	22.09	22.88	23.45	23.96	24.09	23.82
CaO	6.27	7.29	7.04	7.81	6.90	8.33	7.79	8.49	3.05	3.69	4.31	4.87	5.39	5.93	6.29	6.27
Na <sub>2</sub> O	1.71	1.64	1.54	1.30	1.82	0.42	2.27	1.12	9.56	7.54	5.90	4.64	3.70	2.90	2.49	2.71
H <sub>2</sub> O	14.97	13.98	15.77	14.11	15.85	15.26	11.47	13.68	11.00	10.34	9.81	9.43	9.21	9.05	9.09	8.70
Temperature (deg. C)	1049.55	1114.18	1115.12	1139.98	1121.71	1144.74	1168.48	1221.36	1332.97	1349.68	1362.99	1373.08	1380.33	1386.66	1387.76	1389.42
Pressure (bars)	14520.00	17160.00	19140.00	18480.00	19800.00	19140.00	18480.00	24420.00	44880.00	44220.00	43560.00	42900.00	42240.00	41580.00	40920.00	40260.00

(b)

Table 5: Calculated Miyakejima primary magma composition

---

<b>Major Oxides (wt. %)</b>	
<b>SiO<sub>2</sub></b>	51.19
<b>TiO<sub>2</sub></b>	0.95
<b>Al<sub>2</sub>O<sub>3</sub></b>	15.94
<b>FeO*</b>	11.74
<b>MgO</b>	8.13
<b>CaO</b>	9.91
<b>Na<sub>2</sub>O</b>	2.13
<b>H<sub>2</sub>O</b>	1.50

---